Applied Catalysis B: Environmental 259 (2019) 118056

Contents lists available at ScienceDirect

Applied Catalysis B: Environmental

journal homepage: www.elsevier.com/locate/apcatb

Efficient degradation of atrazine with porous sulfurized Fe_2O_3 as catalyst for peroxymonosulfate activation

Han Zheng[a], Jianguo Bao[a,*], Ying Huang[b,c], Luojing Xiang[d], Faheem[a], Bangxing Ren[c], Jiangkun Du[a,*], Mallikarjuna N. Nadagouda[e], Dionysios D. Dionysiou[c,*]

[a] School of Environmental Studies, China University of Geosciences, Wuhan 430074, PR China
[b] College of Chemical and Biological Engineering, Key Laboratory of Biomass Chemical Engineering of Ministry of Education, Zhejiang University, Hangzhou 310027, PR China
[c] Environmental Engineering and Science Program, Department of Chemical and Environmental Engineering, 705 Engineering Research Center, University of Cincinnati, Cincinnati, OH, 45221-0012, United States
[d] Hubei Academy of Environmental Sciences, Wuhan 430072, PR China
[e] Department of Mechanical and Materials Engineering, Wright State University, Dayton, OH, 45324, United States

ARTICLE INFO

Keywords:
Atrazine
Peroxymonosulfate
Porous sulfurized Fe_2O_3
Sulfate radicals
Water treatment

ABSTRACT

In this study, magnetic porous sulfurized Fe_2O_3 (PS-Fe_2O_3) composites were prepared through the co-precipitation method and were applied to activate peroxymonosulfate (PMS) for the degradation of emerging contaminants. Characterization results indicated that PS-Fe_2O_3 catalyst with uniform elemental distribution possessed a large number of micro- and meso- pores. When the molar ratio of $FeSO_4$:$S_2O_3^{2-}$ was 2:1 during the synthesis process, the PS-Fe_2O_3-2 exhibited the best performance on PMS activation for atrazine (ATZ) removal. The catalytic activity of PS-Fe_2O_3 catalysts was enhanced with increased sulfurization extent. The effects of catalyst dosage, PMS concentration, pH, and water impurities (i.e. Cl^-, HCO_3^-, NO_3^- and humic acid) on ATZ degradation were investigated. Both sulfate radicals and hydroxyl radicals were detected in the PS-Fe_2O_3-2/PMS system, and sulfate radicals played the predominant role for the degradation of ATZ. The cycle of ≡Fe(II)/≡Fe(III) and surface-bonded hydroxyl group both contributed to the PMS activation, and the reduction of Fe^{3+} to Fe^{2+} was significantly accelerated by the low-valent sulfur species (such as ≡sulfite) on the catalyst surface. The transformation products of ATZ in PS-Fe_2O_3-2/PMS system were monitored on LC/MS, which were probably generated through lateral chain oxidation and dechlorination-hydroxylation. Overall, PS-Fe_2O_3 has potential to be a feasible catalyst for the removal of organic pollutants from water.

1. Introduction

Atrazine (ATZ) has been widely used as a herbicide to control broad leaf and grassy weeds in agriculture [1]. However, ATZ has been listed as an endocrine disrupter and a probable human carcinogen [2]. In addition, exposure to ATZ has been confirmed to cause negative effects to the reproductive system of amphibians and mammals, such as frog and mice [3,4]. Although ATZ has been restricted in European Union, it is still widely used in North America and China [1,5,6], and is frequently detected in water and soils [7–9]. Unfortunately, ATZ cannot be easily removed from water by adsorption, filtration, coagulation, and biodegradation [10–14]. Therefore, it is necessary to develop reliable treatment processes to eliminate ATZ from the contaminated aqueous systems.

Sulfate radical ($SO_4^{\cdot -}$) based advanced oxidation processes (SR-AOPs) has been recognized as a potentially effective remediation technology for water treatment [15,16]. In comparison with hydroxyl radical ($^{\cdot}OH$), sulfate radical ($SO_4^{\cdot -}$) exhibits similar oxidation ability (2.5–3.1 V NHE vs 1.8–2.7 V NHE of $^{\cdot}OH$), longer half-life time (30–40 μs vs 20 ns of $^{\cdot}OH$), and a better selective oxidation for specific functional organic groups [15,17,18]. These merits make $SO_4^{\cdot -}$-based oxidation process a good supplement to $^{\cdot}OH$-based AOPs in terms of diverse reactivity, product pattern, and energy efficiency [15,19]. $SO_4^{\cdot -}$ can be produced via activating peroxymonosulfate (PMS), which is normally stable without activation [20]. PMS as one of the most common persulfate salts is believed to be more easily catalytically decomposed due to its unsymmetrical structure and shorter bond length of O—O [21]. Typically, PMS can be activated in presence of transition metals [22,23], ultraviolet radiation [24], ultrasound [25], metal-free heterogeneous catalysts [26,27], and inorganic anions like base [28],

* Corresponding authors.
E-mail addresses: bjianguo@cug.edu.cn (J. Bao), dujk@cug.edu.cn (J. Du), dionysios.d.dionysiou@uc.edu (D.D. Dionysiou).

https://doi.org/10.1016/j.apcatb.2019.118056
Received 1 May 2019; Received in revised form 30 July 2019; Accepted 3 August 2019
Available online 10 August 2019
0926-3373/

and phosphates [29,30]. As reported by Anipsitakis and Dionysiou [22], PMS can be activated by transition metals and the efficiency at the conditions they examined and the order of reactivity was: $Ni^{2+} < Fe^{3+} < Mn^{2+} < V^{3+} < Ce^{3+} < Fe^{2+} < Ru^{3+} < Co^{2+}$. However, the homogeneous systems with transition metals have shortcomings, such as toxicity of transition metals to ecosystems, pH limitations, and difficulties in catalyst separation and recovery. Consequently, developing heterogeneous catalysts are highly desirable, which can be easily separated from the aqueous system and are less harmful to the environment for activation PMS.

Iron is a safe, inexpensive and easily available metal element [31,32]. Iron-based catalysts, such as iron oxides (e.g. Fe_2O_3, Fe_3O_4) and zero valent iron (ZVI) have been demonstrated to be feasible catalysts in PMS activation [33–35]. However, the Fe^{3+} species and the slow Fe^{2+} regeneration on the surface of Fe_2O_3 leads to poor activation efficiency [15]. Therefore, many improvements have been made by increase of catalyst loading [36] and modification with an electron transfer mediator [37]. Recently, much scientific attention has been paid to sulfur modified iron-based materials for wastewater treatment [38]. Therein, sulfidation of nZVI (S-nZVI) showed a much higher activity than nZVI in activating persulfate (PDS), H_2O_2, or oxygen for contaminant degradation [39]. Sulfur doping of hematite could reduce the band gap energy of hematite [40]. Additionally, S-doped-Fe_2O_3 has been demonstrated to be a good heterogeneous catalyst in the activation of H_2O_2 under UV or visible light irradiation [41]. Our previous studies found that sulfur-modified iron oxide possess higher reactivity on H_2O_2 or PDS activation compared to non-modified materials [42,43]. Sulfurization in advanced oxidation processes is believed to promote electron transfer between the oxidant and iron species at the material surface, thereby enhancing the activation of H_2O_2 or PDS [39,41–43]. However, the massive iron ions leaching and the pH decreased by the self-control were always a big problem, which means that the long-term stability of the catalyst catalytic efficiency cannot be guaranteed except in the acidic environment or adding reducing agent [42,43]. Therefore, it is worth to investigate the effect of sulfurization on hematite with different modification degree for PMS activation under pH control and subsequent degradation of organic contaminants, which has not yet been adequately studied.

In this study, a porous sulfurized Fe_2O_3 (PS-Fe_2O_3) composite with magnetic property were fabricated via a simple co-precipitation and calcination approach using thiosulfate as the sulfurizing agent. The material was employed to catalyze PMS for the degradation of ATZ under neutral condition. The catalytic activity was dramatically enhanced compared to non-sulfurized Fe_2O_3. The main objectives of this study were to: (1) evaluate the effects of calcination temperature, sulfurization degree, catalyst dosage, PMS concentration, pH, and water impurities on ATZ degradation in the PS-Fe_2O_3/PMS system, (2) study the mechanisms of PMS activation by the PS-Fe_2O_3 and radical generation, and (3) propose the potential degradation pathways of ATZ in the PS-Fe_2O_3/PMS system.

2. Material and methods

2.1. Chemicals and reagents

Atrazine, 5,5-Dimethyl-1-pyrroline N-oxide (DMPO, ESR-spectroscopy), oxalic acid ($C_2H_2O_4$, 98%), and peroxymonosulfate ($KHSO_5{\cdot}0.5KHSO_4{\cdot}0.5K_2SO_4$) were of analytical grade, and $FeSO_4{\cdot}7H_2O$ and $Na_2S_2O_3{\cdot}5H_2O$ were ACS reagents supplied by Sigma-Aldrich. Benzoic acid (BA), Na_2HPO_4, $NaH_2PO_4{\cdot}2H_2O$ and tert-butyl alcohol (TBA) were purchased from Aladdin. Methanol (MeOH) and acetonitrile were of HPLC grade provided by Fisher.

2.2. Preparation of PS-Fe_2O_3 catalyst

Porous sulfurized Fe_2O_3 (PS-Fe_2O_3) materials were synthesized by a coprecipitation and annealing process modified from our previous study [42]. Typically, 20 mmol oxalic acid was dissolved in 50 mL ultrapure water at 60 ℃ under continuous magnetic stirring. Then, 50 mL of 10 mmol $FeSO_4{\cdot}7H_2O$ and a specified stoichiometric ratio of $Na_2S_2O_3{\cdot}5H_2O$ were mixed at 25 ℃, and added dropwise to react with oxalic acid under vigorous stirring at 60 ℃. Yellow precipitates were generated after maintaining over 20 min. The solid precipitate (referred in the manuscript as precursor) was then washed, dried and annealing treated at 350 ℃ for 2 h, and named as PS-Fe_2O_3-X. The character X represents the molar ratio between $FeSO_4{\cdot}7H_2O$ and $Na_2S_2O_3{\cdot}5H_2O$. In this study, four types of PS-Fe_2O_3-X particles (X = 1, 2, 5, 10) were synthesized and evaluated for PMS activation. Unless otherwise specified, the PS-Fe_2O_3 catalyst used in all of the degradation experiments were prepared at 350 ℃.

2.3. Characterization

The surface morphology of PS-Fe_2O_3-X samples was characterized by a scanning electron microscope (SEM, FEI SCIOS). The element composition and crystal structure were investigated on SEM-EDX (ESEM, Quanta 200) and X-ray diffraction (XRD, PANalytical) instruments, respectively. Fourier transform infrared spectra (FTIR) were obtained with a Thermo Fisher spectrometer (Nicolet-6700). Raman spectra were collected from a Renishaw Raman microscope system (RM-1000) equipped with an argon ion laser source ($\lambda = 532$ nm) with a laser power of 22 mW. The Brunauer–Emmett–Teller (BET) surface area was evaluated with a TriStar 3000 analyzer. The magnetic data were tested by a vibrating sample magnetometer (VSM, Quantum Design, PPMS-9) at 300 K. The changes of surface elemental oxidation states were determined on an X-ray photoelectron spectroscope (XPS) (ThermoFisher, Escalab 250XI). The Zeta potential of as prepared catalyst under different pH conditions were characterized with Zeta potential analyzer (NanoBrook Omni).

2.4. Experimental procedures

All experimental tests were conducted in 250 mL beakers under mechanical stirring. The reaction system contained 100 mL of 5 μM ATZ solution as well as 10 mM phosphate buffer to control the pH. Before starting the reaction, a desired amount of PS-Fe_2O_3 materials was added into ATZ solution, and followed by adding a predetermined volume of PMS (100 mM) to initiate the reaction. During the reaction process, 1.0 mL of aqueous sample was withdrawn at selected time intervals, and immediately quenched by 1.0 mL MeOH, and then filtered by 0.22 μm nylon syringe filters, and analyzed by HPLC to determine the concentration of residual ATZ.

In this study, the influence of operation parameters on ATZ degradation in the PS-Fe_2O_3/PMS system was conducted by investigating the single factors as well as the response surface methodology (RSM) model. The single factor experiments including the impact of sulfurization degree (presented with different molar ratio of $FeSO_4{\cdot}7H_2O$ and $Na_2S_2O_3{\cdot}5H_2O$), catalyst dosage, PMS concentration, and pH on ATZ degradation. Based on single factor experiments provided the main influencing factors and their horizontal ranges, the RSM model were built and applied to describe the interactive relationship of experimental parameters. According to the previous literatures [44–46], Central Composite Design (CCD) exhibited excellent performance in building RSM model. The RSM model was fitted on Design-Expert Software (version 11.0).

To explore the influence of homogeneous reaction induced by ion-leaching, a solution containing leached Fe ions was collected after 40 min mechanical stirring of the ATZ reaction solution, containing 5 μM ATZ, 0.4 $g{\cdot}L^{-1}$ PS-Fe_2O_3-2 at pH 7.0 buffered with 10 mM phosphate. Then, PMS was added into the above Fe leaching solution (100 mL) to initiate the homogeneous degradation of ATZ.

2.5. Analytical methods

The residual ATZ was analyzed using a RIGOL L-3000 HPLC equipped with a UV detector at 222 nm, and an Agilent C18 reverse phase column (150 mm x 4.6 mm, 5 mm). The column temperature was set at 30 ℃. The mobile phase was acetonitrile-ultrapure water (60:40, v/v) at a 0.4 mL min^{-1} flow rate.

The transformation products of ATZ were detected using an ultra-high performance liquid chromatography (UHPLC, UltiMate 3000, Dionex) coupled with a mass spectrometer (MS, Q Exactive Hybrid Quadrupole-Orbitrap, Thermo Scientific, Bremen, Germany) with a Hypersil Gold C18 column (3 mm × 150 mm × 3.0 μm, Thermo Fisher) at 30 °C. The MS was operated in the positive mode and measured from 50 *m/z* to 350 *m/z*. The mobile phase for the gradient elution was consisted of 0.1% formic acid solution and acetonitrile at a flow rate of 0.3 mL min^{-1}. The gradient was set to linearly increase from 0% B to 5% B in the first 2 min, then followed by 5% B to 80% B in 8 min, and maintained at 80% B for 6 min, and then returned to 5% B in 2 min, at last kept at 5% B for 2 min.

The amount of the leached Fe ions from catalysts was determined by 1,10-phenanthroline spectrophotometry method at 510 nm [47].

3. Results and discussion

3.1. Characterization

As shown in the SEM images presented in Fig. 1a, the PS-Fe_2O_3-2 samples were micrometer-scale particles in cubic shape with rich cracks and holes (Fig. 1b). The element composition obtained from the EDX analyses clearly indicated that iron, oxygen, and sulfur elements existed in PS-Fe_2O_3-2, and uniformly distributed on the surface of material (Fig. 1d-f). The ratio of Fe, O and S atom on the selected filed of the materials were measured as 38.50%, 58.65% and 2.85%, respectively (Table S1).

The XRD spectra of as-prepared samples are presented in Fig. 2. Before the annealing process, the PS-Fe_2O_3-2 (precursor) samples can be indexed to iron oxalate as shown in Fig. 2a, indicating a good precipitation of ferrous ions. After annealing treatment, iron oxalate would decompose and convert to iron oxides. The typical diffraction peaks of PS-Fe_2O_3-2 observed at 30.2°, 35.7°, 43.9°, 54.2°, 57.6°, and 62.9° could be mainly matched with γ-Fe_2O_3 phase (JCPDS: No. 24-0081). The peaks at 24.2°, 33.2°, and 49.5° belonged to α-Fe_2O_3 phase (JCPDS: No. 33-0664). The results indicated that the α- and γ-Fe_2O_3 phase coexisted in the PS-Fe_2O_3-2.

In addition, the XRD patterns of PS-Fe_2O_3-2 composites obviously changed compared to the spectrum of Fe_2O_3 (Fig. 2a). Several new peaks formed, such as 18.1°, 27.4° exhibited the formation of butlerite (JCPDS No. 23-0304). The intensity of the peak at 33.2° was greatly weakened. These structural changes might be attributed to the phase transformation in PS-Fe_2O_3-2 preparation [43]. Fig. 2b was XRD patterns of as prepared PS-Fe_2O_3 with different ratio of $FeSO_4$•$7H_2O$ to $Na_2S_2O_3$•$5H_2O$, reflecting the sulfurization effect on the structural properties of PS-Fe_2O_3 composites. When the ratio of $FeSO_4$•$7H_2O$ to $Na_2S_2O_3$•$5H_2O$ increased, the peaks indexed to butlerite, α-Fe_2O_3 and γ-Fe_2O_3 phase almost vanished, indicating that Fe_2O_3 was converted to other iron oxides [43].

As depicted in Fig S2a, the Raman spectra of PS-Fe_2O_3 at peaks of 216 cm^{-1}, 281 cm^{-1}, 391 cm^{-1}, 488 cm^{-1}, 595 cm^{-1}, 653 cm^{-1}, 815 cm^{-1} and 1299 cm^{-1} were assigned to hematite (α-Fe_2O_3) phase [41,48,49]. This further proves the existence of α phase Fe_2O_3 in the material, indicating that α- and γ phase Fe_2O_3 coexist in PS-Fe_2O_3-2. In addition, a new Raman peak at 1076 cm^{-1} was found and could be assigned to surface-bounded SO_4^{2-} [41], which was generated from material sulfurization.

The Fe_2O_3 and PS-Fe_2O_3-2 samples were characterized by FTIR to monitor the influence of sulfurization on the surface functional groups of synthesized materials. As shown in Fig. S2b, the FTIR spectra of PS-Fe_2O_3-2 is different to that of Fe_2O_3 in two ways. On the one hand, new bands at 1488 cm^{-1}, 1127 cm^{-1} were detected in PS-Fe_2O_3-2, which could be ascribed to the S—O stretching motion of surface bonded sulfite and sulfate [50,51]. On the other hand, the bands at 535 cm^{-1}, 456 cm^{-1} attributed to Fe—O vibration blue shifted to 594 cm^{-1}, 458 cm^{-1} in PS-Fe_2O_3-2. The results indicated that sulfurization would generate new defects inside the iron oxide structure [52], which might facilitate electron transfer in catalyst [53].

The BET surface area and pore volume of PS-Fe_2O_3-2 were about

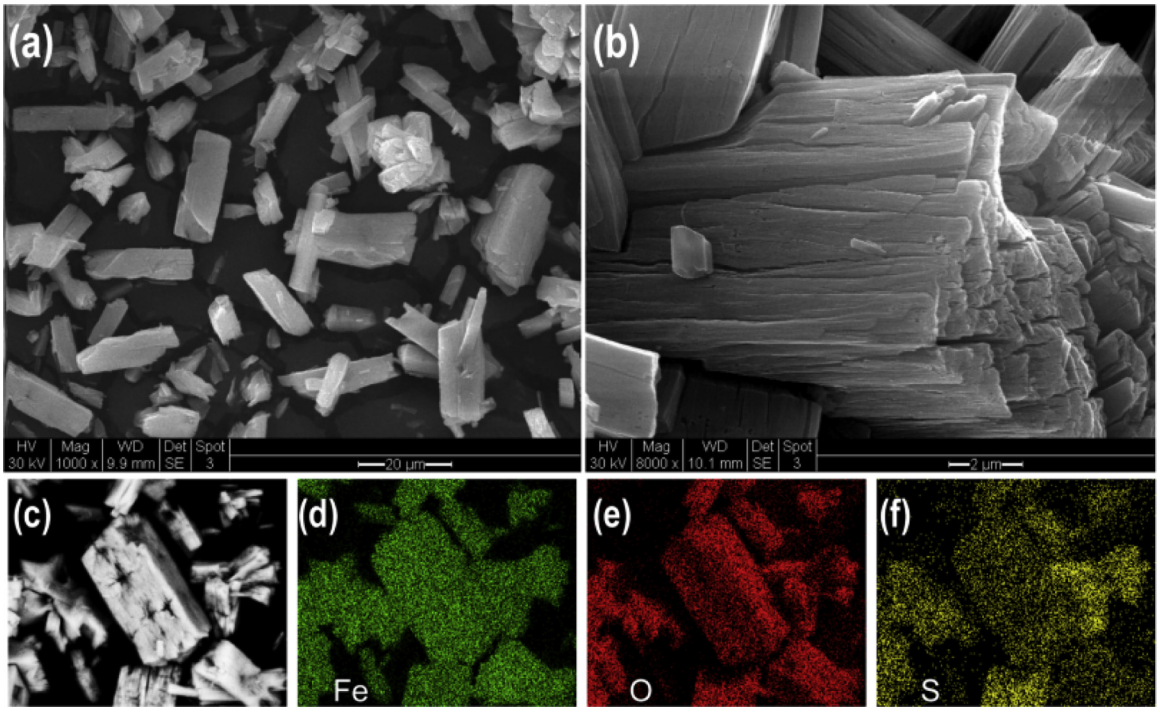

Fig. 1. (a,b) SEM images of the prepared PS-Fe_2O_3-2; (c–f) EDX mapping of Fe, O, and S elements of the selected PS-Fe_2O_3-2 from (c).

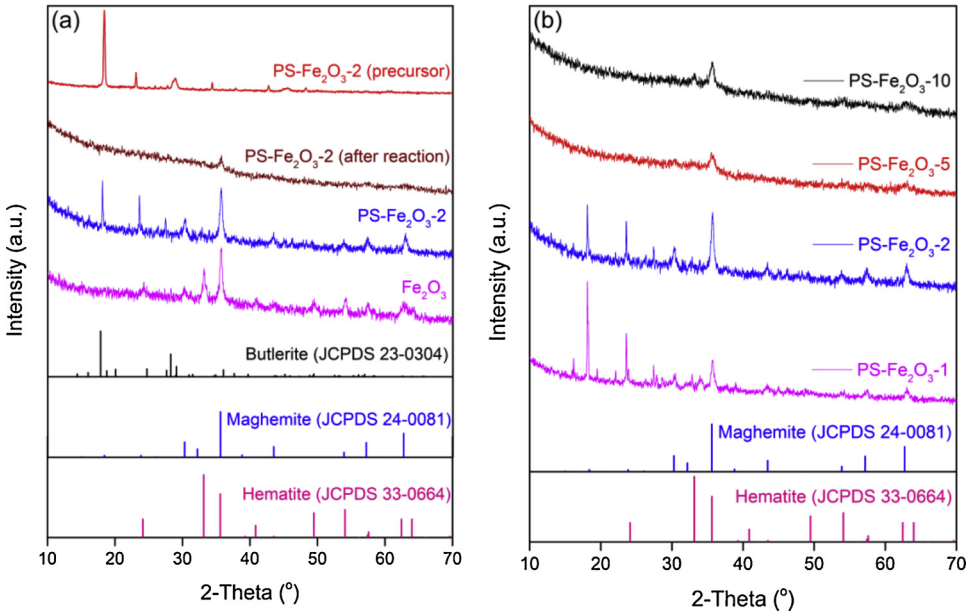

Fig. 2. XRD patterns of (a) Fe_2O_3, PS-Fe_2O_3-2, PS-Fe_2O_3-2 (after reaction), PS-Fe_2O_3-2 (precursor), and (b) as prepared PS-Fe_2O_3 composites.

134.0 m^2/g and 0.222 cm^3/g, suggesting mesoporous and macroporous structure in the materials (Fig. S3). The saturation magnetization value of PS-Fe_2O_3-2 were identified as 12.7 emu·g^{-1}, indicating the good magnetic property and the easy recovery by an external magnet (Fig. S4 and insert).

3.2. Catalytic degradation of ATZ by various reaction systems

The catalytic performances of different reaction systems on ATZ degradation are illustrated in Fig. 3. In the presence of PS-Fe_2O_3-2 alone, less than 4% of ATZ was adsorbed onto the catalyst surface within 40 min reaction. In the system with only 0.6 mM PMS, about 14% of ATZ was removed, which might be due to the PMS activation by phosphate anions at neutral pH [29]. Therefore, systems without PS-Fe_2O_3-2 or PMS could not result in significant ATZ removal. In contrast, 96% of ATZ was degraded within 40 min in systems comprising both of PS-Fe_2O_3-2 and PMS. Moreover, the ATZ degradation within the first 30 min could be well fitted by the pseudo-first-order kinetics with a reaction rate constant of 0.099 min^{-1}. Furthermore, only 17% of the ATZ was degraded in the homogeneous leached Fe/PMS system,

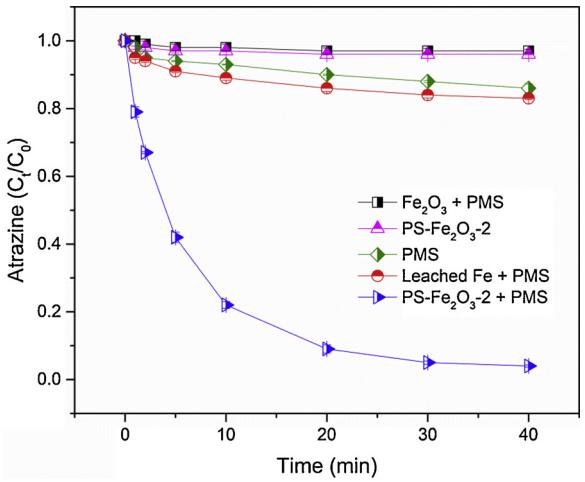

Fig. 3. ATZ degradation in various reaction systems. Conditions: $[catalyst]_0$ = 0.4 g·L^{-1}, $[PMS]_0$ = 0.6 mM, $[ATZ]_0$ = 5 μM, pH = 7.0.

implying that the heterogeneous activation of PMS by PS-Fe_2O_3-2 catalyst plays the dominant role in the ATZ degradation.

ATZ was slightly degraded by Fe_2O_3/PMS system, indicating that Fe_2O_3 had limited reactivity towards PMS activation under neutral pH controlled by phosphate buffer. As previously reported, phosphate ions can significantly inhibit the performance of Fe_2O_3 on PMS activation [33], and ≡Fe(III) on the surface of Fe_2O_3 exhibited low reactivity for PMS activation with phosphate buffer [54]. Similarly, the performance of the PS-Fe_2O_3-2/PMS system was also suppressed in the presence of phosphate buffer (Fig. S5a). The reason is that phosphate could replace the surface hydroxyl groups of the catalyst by complexing with surface ≡Fe(III), resulting in the decrease of the PMS active site [55]. However, PS-Fe_2O_3-2 still exhibited higher catalytic activity than Fe_2O_3 in PMS activation.

3.3. Influence of key factors

3.3.1. The effects of calcination temperature, sulfurization degree

To evaluate the effect of calcination temperature on catalyst catalytic activity, the PS-Fe_2O_3-2 precursors were thermally treated at 250 °C, 350 °C, 450 °C, 550 °C for 2 h, respectively, and named by the calcination temperature. As shown in Fig. 4a, the catalyst activity firstly enhanced when the calcination temperature increased from 250 °C to 350 °C, and then decreased across 450 °C to 550 °C. According to the first-order reaction rate constants (k) summarized in Table S3, the catalytic properties of samples treated at different temperature followed the order of 350 °C > 250 °C > 450 °C > 550 °C.

According to the XRD results depicted in Fig. S6, this phenomenon should be attributed to the following reasons: (1) when the calcination temperature was 250 °C, the obtained catalyst has amorphous phase, indicating the ferrous oxalate precursor was not fully calcined to generate large numbers of available active sites for PMS activation. (2) When the calcination temperature increased to 350 °C, the precursor was sufficiently calcined and converted to Fe_2O_3 with α-phase and γ-phase coexisted as α-γ phase junctions, in which new active sites related to PMS activation maybe generated by this α-γ phase junctions generation [56]. (3) When the calcination temperature was enhanced from 350 °C to 450 °C and 550 °C, respectively, the crystal structure was converted from α-γ phase junctions to α-Fe_2O_3 phase at 450 °C, and further became to be 100% pure hematite phase at 550 °C. At the same time, the catalytic effect of the material was reduced. Because

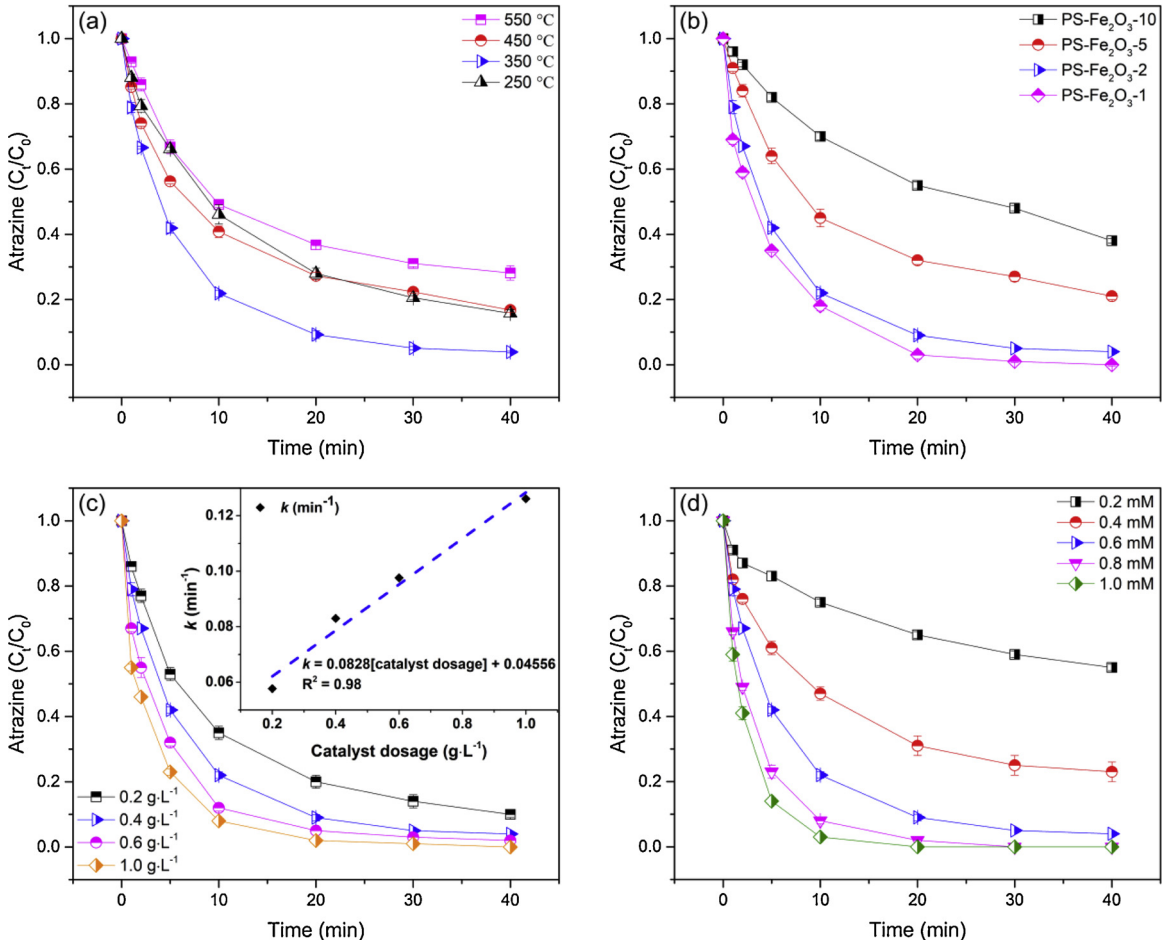

Fig. 4. The effect of (a) calcination temperature; (b) sulfurization degree; (c) catalyst dosage; and (d) PMS concentration on ATZ degradation in the PS-Fe_2O_3/PMS system. General conditions: $[catalyst]_0 = 0.4\ g{\cdot}L^{-1}$, $[PMS]_0 = 0.6\ mM$, $[ATZ]_0 = 5\ \mu M$, pH = 7.0.

calcination the PS-Fe_2O_3-2 precursor at high temperature is conducive to form a more stable crystal phase, thus reducing the active site of the catalyst. Therefore, the efficient removal of ATZ by the PMS/PS-Fe_2O_3-2 (calcinated at 350 ℃) might be attributed to the high catalytic ability of the γ-Fe_2O_3 phase in the PS-Fe_2O_3-2.

As depicted in Fig. S7, the oxalate precursor showed well performance on the catalytic PMS oxidation of ATZ, but the reaction rate was less than PS-Fe_2O_3-2/PMS system and close to the system with only precursor (Table S3). Interestingly, ATZ was hardly removed from the system containing only PS-Fe_2O_3-2. The above results indicated that the precursor had well performance on ATZ removal through adsorption or reduction. On the other hand, the calcination process could ensure the stability of PS-Fe_2O_3-2 in the reaction solution. As seen in Fig. S8, the amount of Fe ions leaching from precursor was $10.22\ mg\ L^{-1}$. After precursor was calcined at 250 ℃, 350 ℃, 450 ℃, and 550 ℃, the dissolved Fe ions was significantly dropped to 4.57, 1.04, 0.7, and $0.34\ mg\ L^{-1}$, respectively. Therefore, in order to achieve the catalyst with highly catalytic activity, low Fe ions leaching, and magnetic performance, the calcination temperature was fixed at 350 ℃.

To investigate the impact of sulfurization degree on the catalytic performance of PS-Fe_2O_3 in PMS oxidation of ATZ, PS-Fe_2O_3 materials prepared from different ratio of $FeSO_4{\cdot}7H_2O$ and $Na_2S_2O_3{\cdot}5H_2O$ were applied in PS-Fe_2O_3/PMS system. As depicted in Fig. 4b, ATZ removal was markedly enhanced with increasing thiosulfate concentration during the process of PS-Fe_2O_3 preparation, which confirmed the activation of PMS by iron oxide can be promoted by sulfurization. It was reported that sulfidation on iron based catalysts could accelerate electron transfer between oxidants and iron species at catalyst's surface [42,43], which might be the reason that the catalytic performance of PS-Fe_2O_3/PMS system was significantly improved by sulfurization.

3.3.2. *The effects of catalyst dosage and PMS concentration*

The effects of catalyst dosage, PMS concentration on ATZ removal were studied. As illustrated in Fig. 4c, the ATZ degradation was improved with an increase in PS-Fe_2O_3-2 dose from $0.2\ g{\cdot}L^{-1}$ to $1.0\ g{\cdot}L^{-1}$. The first-order reaction rate constant (k) increased from $0.057\ min^{-1}$ to $0.126\ min^{-1}$ (Table S3), presenting a linear relation of catalyst dosage in PS-Fe_2O_3-2/PMS system (inset in Fig. 4c). This observation suggested that more catalyst could provide PMS activation with more available active sites and surface area.

In addition, the PMS concentration exerted a positive influence on ATZ degradation (Fig. 4d). When the PMS concentration increased from 0.2 mM to 1.0 mM, ATZ removal in 40 min promoted from 45% to 100%. Accordingly, the reaction rate constant (k) increased significantly from $0.017\ min^{-1}$ to $0.262\ min^{-1}$ as summarized in Table S3. The increase of PMS concentration provided more contact with PS-Fe_2O_3-2, and enhanced ATZ degradation.

3.3.3. *Effects of solution pH*

As previously reported, solution pH can influence the heterogeneous PMS oxidation system by affecting the catalyst surface charge as well as the speciation of PMS and pollutants [20,21]. As shown in Fig. 5, the ATZ removal first increased as the solution pH increased from 4.2 to 9.2, and then greatly decreased at pH 11.2 (12%). The best performance of PS-Fe_2O_3-2/PMS system was observed in neutral and slightly alkaline conditions. The reasons for this result are as follows: (i) H^+ had the

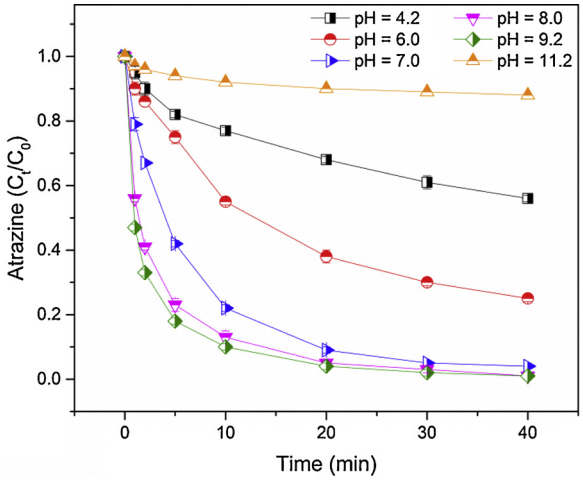

Fig. 5. Effect of solution pH on ATZ degradation. Reaction conditions: [PS-Fe_2O_3-2]$_0$ = 0.4 g·L^{-1}, [PMS]$_0$ = 0.6 mM, [ATZ]$_0$ = 5 μM.

stabilization effect on HSO_5^-, which is the predominant species of PMS (pK_{a1} = 0, pK_{a2} = 9.4) present in solution at pH from 4.2 to 9.2 [57,58]. Moreover, H^+ may form H-bond with O—O group of HSO_5^-, decreasing the interaction between HSO_5^- and positively charged oxide [59]. (ii) The pH_{pzc} of PS-Fe_2O_3-2 was determined to be around 10.2 (Fig. S9), implying that the catalyst was positively charged when solution pH < pH_{pzc} and negatively charged when pH < pH_{pzc}. Additionally, ATZ ($pK_{a\ (ATZ)}$ = 1.7) presented as negative ions in the range of pH from 4.2 to 9.2 [60,61]. The ATZ anions and HSO_5^- would be adsorbed onto PS-Fe_2O_3-2 by electrostatic attraction, facilitating ATZ degradation. (iii) When pH increased to 11.2, which was higher than pH_{pzc}, the negatively charged surface of PS-Fe_2O_3-2 would form an electrostatic repulsion between ATZ anions and PMS in the form of SO_5^{2-}, leading to the reduction of ATZ removal rate. Therefore, the best ATZ degradation efficiency was obtained at pH 9.2. The high degradation rate of PS-Fe_2O_3-2/PMS process at neutral and slightly alkaline solutions suggest that this process has potential to treat surface water.

3.4. Interactive relationship of experimental parameters

In this study, four independent parameters (sulfurization degree, catalyst dosage, PMS concentration, and pH) with 5 levels (-α, -1, 0, +1, +α) were chosen to investigate the ATZ removal efficiency. The details of experiments designed by CCD and measured response values (ATZ removal %), presented in Table S4. After regression analysis, it is concluded that ATZ removal % was in line with the quadratic polynomial relationship with A (PS-Fe_2O_3 dosage), B (PMS dosage), C (pH) and D ($FeSO_4/Na_2S_2O_3$). The prediction formula was described as follows:

ATZ remove % = + 72.4 + 8.17 × A + 8.93 × B + 7.74 × C − 7.53 × D − 2.04 × AB − 0.8567 × AC + 0.9866 × AD − 0.1626 × BC + 1.88 × BD − 0.0365 × CD − 1.2 × A^2 − 0.957 × B^2 − 0.9135 × C^2 + 3.16 × D^2

Model ANOVA (ANOVA) was to investigate the relationship between all variables and response values to ananlyze whether the model hypothesis parameters were meaningful. As shown in Table S5, the F-value and p-value of model were 137.76 and 0.0001, respectively, suggested that the model was significant. The p-value of "lack of fit" was 0.0661 (> 0.05), which was not significant. This indicated that the model could well predicted the results. In addition, the value of R^2 and "Adeq Precision" was 0.9923 and 49.295 (> 4), respectively. It indicated that the model established with RSM exhibited excellent potential in predicting the response value (ATZ remove %) [62].

The 3D response surface plots were utilized to describe the interactive relationships between parameters and responses, when the RSM model was established [44]. As decribled in Table S5, the P values of interaction terms (AB, BD) < 0.05, indicating the relationships between [PS-Fe_2O_3] and [PMS], [PMS] and $FeSO_4/Na_2S_2O_3$ were significant in the PS-Fe_2O_3/PMS system. The relevant 3D response surfaces were shown in Fig S10. Fig. S10a illustrates the interactive relationship between [PS-Fe_2O_3] and [PMS], It can be seen that ATZ removal efficiency would improve gradually with the increase of PS-Fe_2O_3 and PMS dosage. This was due to the increase of PS-Fe_2O_3 and PMS would facilitate the reaction between active sites available in the material and HSO_5^- to continuously formation free radicals. Fig. S10b shows the interactive relationship between [PMS] and $FeSO_4/Na_2S_2O_3$. Reduction the ratio of $FeSO_4/Na_2S_2O_3$ during PS-Fe_2O_3 preparation could activate PMS efficiently, implying the positive correlation between sulfurization degree and peroxymonosulfate (PMS).

3.5. Influence of ionic strength, anions and humic acid

The increase of solution ionic strength would reduce the effect of electrostatic bonding between heterogeneous catalysts and oxidants or pollutants by compressing the thickness of the electric double layers, but maybe ineffective to affect the inner sphere complexation [54]. Fig. 6a exhibits that ATZ degradation was little affected by the presence of $NaClO_4$ at concentrations from 1 mM to 100 mM, implying a strong inner-sphere interaction between HSO_5^- and the active sites on the surface of PS-Fe_2O_3-2, which is not affected by changing ionic strength [55,63]. The interaction was likely originated from the binding or complexation between molecular O in HSO_5^- and active metal sites on catalyst surface as previously suggested in another study [59].

Nitrate, chloride, and bicarbonate are common water anions that may exert influence in ATZ degradation by PS-Fe_2O_3-2/PMS. As shown in Fig. 6b, ATZ removal was not significantly affected by adding 1 mM and 10 mM NO_3^-, but was obviously inhibited with 50 mM and 100 mM NO_3^-. This could be attributed to the quenching effect of NO_3^- on radicals ($SO_4^{\cdot -}$, $^{\cdot}OH$), which would be transformed to less reactive species such as $NO_3^{\cdot}$ and $NO_2^{\cdot}$ through Eqs. (1)–(3) [57].

$$^{\cdot}OH + NO_3^- \rightarrow OH- + NO_3^{\cdot} \quad (1)$$

$$SO_4^{\cdot -} + NO_3^- \rightarrow SO_4^{2-} + NO_3^{\cdot} \quad (2)$$

$$H_2O + e_{aq}^- + NO_3^{\cdot} \rightarrow 2OH^- + NO_2^{\cdot} \quad (3)$$

Fig. 6c shows that the degradation of ATZ in PS-Fe_2O_3-2/PMS system decreased from 96% to 26% with concentration of Cl^- increasing from 0 to 1 mM. This significant inhibition was probably ascribed to the consumption of radicals ($SO_4^{\cdot -}$, $^{\cdot}OH$) or HSO_5^- in the presence of Cl^- with generation of chlorine radicals or hypochlorous species with less reactivity (Eqs. (4)–(8)) [33,64–66]. Bicarbonate is another ubiquitous water constituent with typical concentrations from 50 to 200 mg/L as HCO_3^-, which usually acts as radical scavengers in SR-AOPs [67,68]. As depicted in Fig. 6d, the ATZ degradation in the PS-Fe_2O_3-2/PMS system could be remarkably suppressed in the presence of bicarbonate. ATZ removal gradually decreased from 96% to 21% when HCO_3^- concentration increased from 0 to 4 mM. In the PS-Fe_2O_3-2/PMS system, HCO_3^- would compete for $SO_4^{\cdot -}$ and $^{\cdot}OH$ to yield less active radicals (Eqs. (9) and (10)), thus resulting in the decrease in ATZ degradation as also reported in other relevant studies [57].

$$SO_4^{\cdot -} + Cl^- \leftrightarrow SO_4^{2-} + Cl^{\cdot} \quad (4)$$

$$^{\cdot}OH + Cl^- \leftrightarrow HOCl^{\cdot -} \quad (5)$$

$$HOCl^{\cdot -} + H^+ \leftrightarrow H_2O + Cl^{\cdot} \quad (6)$$

$$HSO_5^- + Cl^- \leftrightarrow SO_4^{2-} + HOCl \quad (7)$$

$$HSO_5^- + 2Cl^- + H^+ \rightarrow SO_4^{2-} + Cl_2 + H_2O \quad (8)$$

$$^{\cdot}OH + HCO_3^- \rightarrow OH^- + CO^{\cdot} \quad (9)$$

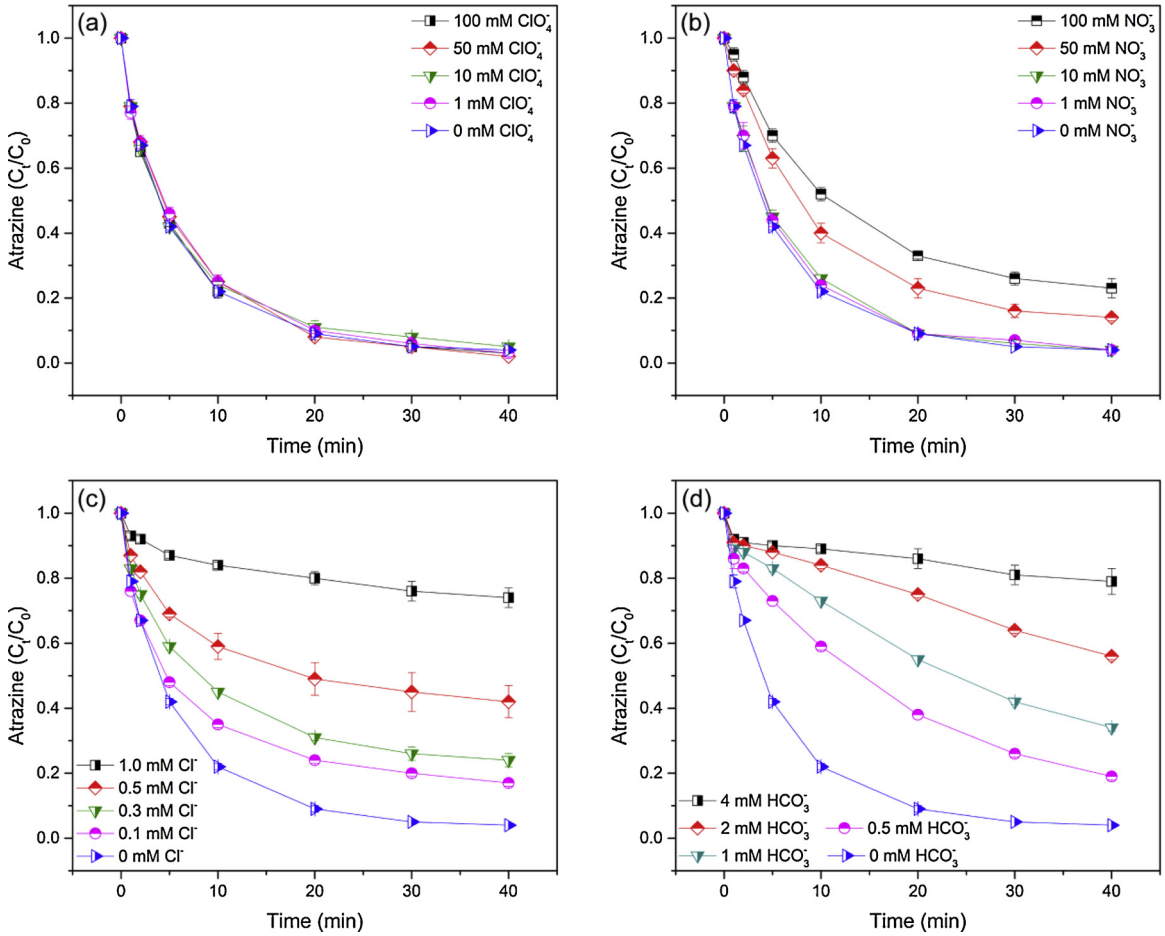

Fig. 6. Effect of inorganic anions on ATZ degradation in PS-Fe_2O_3-2/PMS system: (a) ion strength, (b) nitrate, (c) chloride, (d) bicarbonate. Reaction conditions: [PS-Fe_2O_3-2]$_0$ = 0.4 g·L^{-1}, [PMS]$_0$ = 0.6 mM, [ATZ]$_0$ = 5 μM, pH = 7.0.

$$SO_4^{\cdot -} + HCO_3^- \rightarrow SO_4^{2-} + HCO_3^{\cdot -} \quad (10)$$

The influence of humic acid (HA) as depicted in Fig. S11. ATZ degradation was notably suppressed in the PS-Fe_2O_3-2/PMS system with the addition of HA. In this study, 96% ATZ was removed in the absence of HA, whereas only 74% ATZ was degraded in the presence of 4 mg L^{-1} HA (Fig. S11). These results are attributed to the electron-rich groups of HA, which played a competitive role in the consumption of $SO_4^{\cdot -}$ and ·OH [5,65,69], consequently leading to decrease in ATZ degradation.

3.6. Identification of oxidizing species

In this study, ESR experiments employing the spin-trapping agent (DMPO) were conducted to examine the existence of free radicals involved in PS-Fe_2O_3-2/PMS system at different time [15]. Fig. 7a shows that PMS alone in the absence of DMPO and DMPO alone were unable to evoke any EPR signal. However, the combination between DMPO with PMS would generate an EPR signal in terms of 1:2:1:2:1:2:1 heptet (A_N = 0.72 m T, A_H(2 H) = 0.42 m T), which was assigned to DMPOX adducts [70,71]. According to previous reports [72–74], the appearance of DMPOX adducts might be attributed to strong oxidizing species (e.g. $SO_4^{\cdot -}$ and ·OH) induced over-oxidation of DMPO. The signal of DMPOX detected in PMS alone system was consistent with the result that PMS could be activated by phosphate anion to produce active species at neutral pH as depicted in Fig. S5b. This conclusion was consistent with previous reports [29,57].

When DMPO was added to PS-Fe_2O_3-2/PMS system with 5 μM ATZ, as shown in Fig. 7b, the EPR spectra peaks of DMPO-·OH adducts and DMPO-$SO_4^{\cdot -}$ adducts were clearly evidenced, confirming the presence of both ·OH and $SO_4^{\cdot -}$ radicals during the catalytic activation of PMS with PS-Fe_2O_3-2. Additionally, the intensities of DMPO-·OH and DMPO-$SO_4^{\cdot -}$ were enhanced in five-min reaction compared to that in one-min reaction, indicating that ·OH and $SO_4^{\cdot -}$ radicals were produced in the ATZ degradation process by PS-Fe_2O_3-2/PMS system. Besides, the residual EPR spectral peaks in Fig. 7b contained a triple peak with an intensity ratio of 1:1:1, which was attributed to the by-product peak formed by further oxidation of DMPO-•OH adducts in the system [70].

3.7. Studies for the main radical species in PS-Fe_2O_3-2/PMS system

To reveal the roles of ·OH and $SO_4^{\cdot -}$ on ATZ degradation, the radicals quenching experiments were carried out employing methanol (MeOH) and tert-butyl alcohol (TBA) as scavengers. Based on the reaction rate constants of ·OH and $SO_4^{\cdot -}$ with ATZ, MeOH and TBA (summarized in Table S6), MeOH could scavenge both ·OH and $SO_4^{\cdot -}$, and TBA could quench ·OH [15]. Fig. 7c depicts that the ATZ removal was significantly inhibited by alcohols compared to the systems without addding alcohol. When the reaction system was spiked with MeOH, ATZ degradation was remarkably suppressed by 30–60 mM MeOH. However, the degradation efficiency of ATZ was only reduced from 46% to 37% when the concentration of TBA increased from 30 mM to 60 mM. The above results suggested that both ·OH and $SO_4^{\cdot -}$ were generated in the PS-Fe_2O_3-2/PMS system and $SO_4^{\cdot -}$ might be the main radical for ATZ degradation.

In addition, to further understand the contributions of ·OH and $SO_4^{\cdot -}$ radicals in the PS-Fe_2O_3-2/PMS/ATZ system, competition kinetic

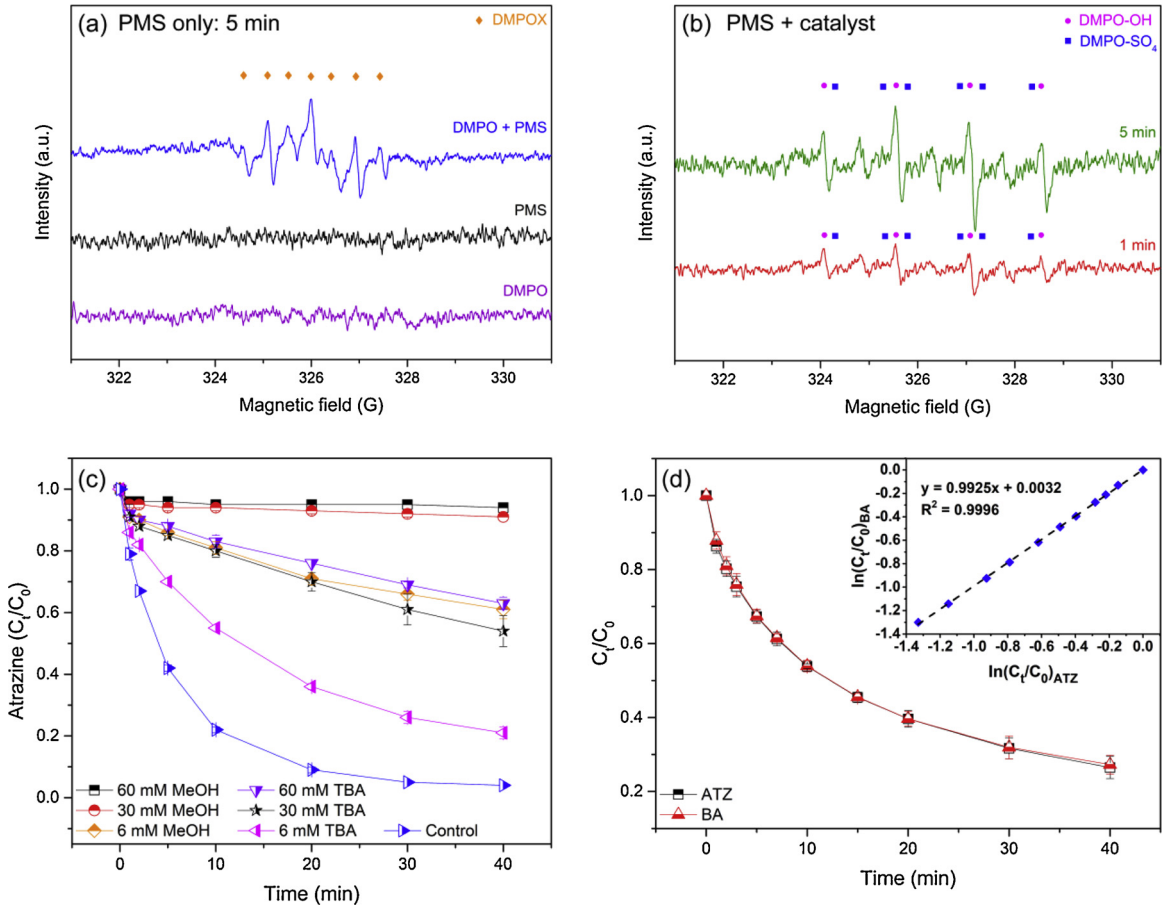

Fig. 7. (a, b) EPR spectra of various conditions ($[ATZ]_0$ = 5 μM, $[PMS]_0$ = 0.6 mM, DMPO = 0.1 M, $[PS\text{-}Fe_2O_3\text{-}2]_0$ = 0 or 0.4 g·L^{-1}, pH = 7.0. : DMPOX; DMPO−OH; DMPO-SO_4); (c) Effect of quenching agents on ATZ removal ($[ATZ]_0$ = 5 μM, $[PMS]_0$ = 0.6 mM, $[PS\text{-}Fe_2O_3\text{-}2]_0$ = 0.4 g·L^{-1}, pH = 7.0); (d) Competition kinetics between ATZ and BA with reactive species in PS-Fe_2O_3-2/PMS system ($[ATZ]_0$ = $[BA]_0$ = 5 μM, $[PMS]_0$ = 0.6 mM, $[PS\text{-}Fe_2O_3\text{-}2]_0$ = 0.4 g·L^{-1}, pH = 7.0).

experiments at the same concentration of benzoic acid (BA) and ATZ were conducted on the base of previous reports [75,76]. We assumed that both ATZ and BA could be degraded by ·OH or $SO_4^{\cdot-}$ and the degradation of ATZ and BA should follow the relationship provided by Eqs. (11) or (12):

$$\frac{\ln[\frac{Ct,BA}{C0,BA}]}{\ln[\frac{Ct,ATZ}{C0,ATZ}]} = \frac{kBA,\ ^{\cdot}OH}{kATZ,\ ^{\cdot}OH} \quad (11)$$

$$\frac{\ln[\frac{Ct,BA}{C0,BA}]}{\ln[\frac{Ct,ATZ}{C0,ATZ}]} = \frac{kBA,\ SO_4^{\cdot-}}{kATZ,\ SO_4^{\cdot-}} \quad (12)$$

Here $C_{0,\ BA}$, $C_{0,\ ATZ}$ and $C_{t,\ BA}$, $C_{t,\ ATZ}$ are the initial and t reaction time concentrations of BA and ATZ, respectively; $k_{BA,\ \cdot OH}$ and $k_{ATZ,\ \cdot OH}$ are the rate constants of BA and ATZ with ·OH, respectively; $k_{BA,\ SO4\cdot-}$ and $k_{ATZ,\ SO4\cdot-}$ are the rate constants of BA and ATZ with $SO_4^{\cdot-}$, respectively. The value of $k_{BA,\ \cdot OH}$, $k_{ATZ,\ \cdot OH}$, $k_{BA,\ SO4\cdot-}$ and $k_{ATZ,\ SO4\cdot-}$ are summarized in Table S6. The results calculated from k above are as follows: $k_{BA,\ \cdot OH}/k_{ATZ,\ \cdot OH}$ = 1.97, and $k_{BA,\ SO4\cdot-}/k_{ATZ,\ SO4\cdot-}$ = 0.5. Theoretically, If ATZ removal is mainly induced by ·OH or $SO_4^{\cdot-}$, the k_{BA}/k_{ATZ} should close to 1.97 or 0.5, respectively. k_{BA} and k_{ATZ} were the observed degradation rate constants of BA and ATZ in the PS-Fe_2O_3-2/PMS system. The degradation curves of BA and ATZ and their competitive dynamics fitting results are illustrated in Fig. 7d. The slope of the linear fitting (inset in Fig. 7d) demonstrated that the ratio of k_{BA}/k_{ATZ} was about 0.9925, closing to $k_{BA,\ SO4\cdot-}/k_{ATZ,\ SO4\cdot-}$ (0.5), and away from $k_{BA,\ \cdot OH}/k_{ATZ,\ \cdot OH}$ (1.97). The results indicated that both ·OH and $SO_4^{\cdot-}$ contributed to the degradation of ATZ, and $SO_4^{\cdot-}$ played the dominant role.

3.8. Catalytic mechanism and stability of the PS-Fe_2O_3-2/PMS process

3.8.1. Proposed catalytic mechanism of the PS-Fe_2O_3-2/PMS process

It was reported that the generation of $SO_4^{\cdot-}$ by transition metal based heterogeneous activation of PMS was related to the metallic redox conversion as well the involvement of surface −OH groups [23,77,78]. Moreover, the sulfur-containing species on PS-Fe_2O_3-2 surface might involve in PMS activation, due to the inferior catalytic ability of bare Fe_2O_3 without S doping. It has been confirmed that sulfur-containing species worked as electron donor for PDS or PMS activation by sulfur-containing iron based catalyst [43,79].

As presented in Fig. 8a, the FTIR spectra bands at 1488 cm^{-1} and 1127 cm^{-1} for the fresh PS-Fe_2O_3-2 were attributed to the S—O stretch vibration of surface-bonded sulfite and sulfate, respectively [50,51]. The bands at 594 cm^{-1} and 458 cm^{-1} were assigned to the Fe(III) − O stretch vibration. For the PS-Fe_2O_3-2 after reactions, the S—O signal red-shifted to 1485 cm^{-1} and 1022 cm^{-1} and the Fe(III) − O signal red-shifted to 551 cm^{-1} and 458 cm^{-1}, indicating the simultaneous involvement of surface sulfite/sulfate and ≡Fe(III) in the PMS activation processes. The results suggested the electrons transfer among the surface-bonded sulfite/sulfate, the neighboring ≡Fe(III), and surface-bonded PMS during the reactions, which could accelerate the ≡Fe(III)/≡Fe(II) cycling and promote the PMS activation [54].

To further investigate the role of sulfur and iron species in PS-Fe_2O_3-2 catalyst for the PMS activation, the chemical state and proportion of the surface elements, C, O, Fe, S elements, on the fresh and used PS-Fe_2O_3-2 were investigated using XPS (Fig. S12). The relative atomic

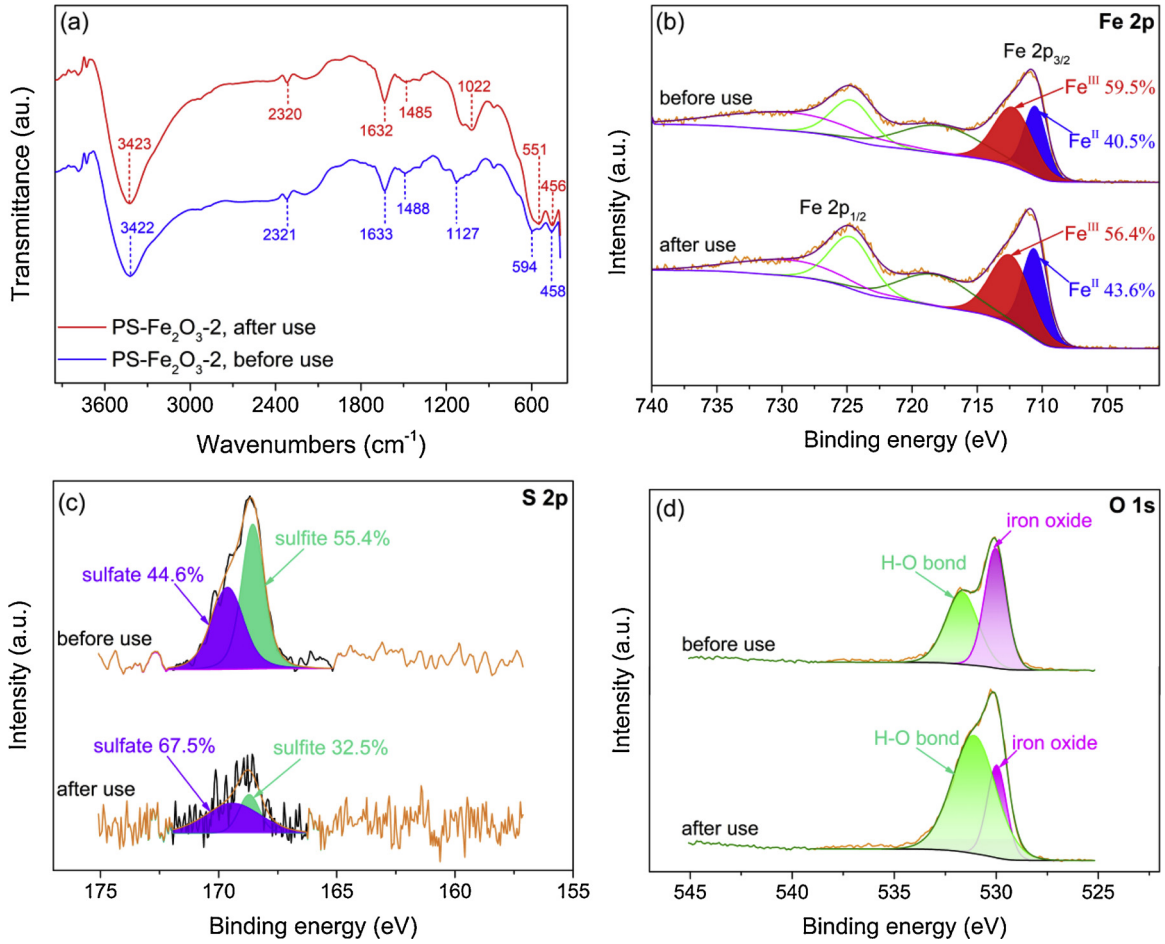

Fig. 8. (a) FTIR spectra, and XPS spectra of (b) Fe 2p, (c) S 2p, (d) O 1s of PS-Fe_2O_3-2 before and after use in the PS-Fe_2O_3-2/PMS system.

ratios of Fe 2p, O1 s and S 2p in fresh PS-Fe_2O_3-2 were 20.51%, 54.64% and 3.83%, respectively. The results were consistent with the results of EDX. The relative atomic ratios of Fe 2p, and S 2p in used PS-Fe_2O_3-2 were significantly decreased, due to the consumption of iron and sulfur during PMS activation for ATZ oxidation. The Fe 2p spectra in fresh PS-Fe_2O_3-2 catalyst (Fig. 8b) at 710.5 eV and 712.2 eV was attributed to the Fe 2p3/2 of Fe(II) and Fe(III) [80,81], accounting for 40.5% and 59.5%, respectively. For the spectrum of Fe 2p in used PS-Fe_2O_3-2, the relative content of Fe(II) and Fe(III) peaks were 43.6% and 56.4%, respectively. The results implied that both Fe(II) and Fe(III) participated in the PMS activation, and the presence of Fe(II)/Fe(III) cycle on the PS-Fe_2O_3-2 surface. On the contrary, the relative content of Fe(II) decreased in the Fe_2O_3/PMS system (Fe(II) account for 33.2% before use and 32.9% after use in Fig.S13). The variation suggests that sulfurization of Fe_2O_3 accelerated the Fe(II)/Fe(III) cycle through electron transfer.

As depicted in Fig. 8(c), the XPS spectra of S 2p peaks of the fresh PS-Fe_2O_3-2 could be fitted into two peaks with binding energy positioned at 168.5 and 169.6 eV, corresponding to surface bond sulfite and sulfate [42,82], which accounted for 55.4% and 44.6%, respectively. After the reaction, the S 2p peak decreased to some extent and the relative peak content of sulfite and sulfate were 32.5% and 67.5%, respectively, indicating the transformation of sulfite to sulfate. Thas was due to the fact that the sulfite on the surface of PS-Fe_2O_3-2 acted as electron donor to promote Fe(II) regeneration for PMS activation.

The XPS spectra of O 1s in the fresh and used PS-Fe_2O_3-2 are shown in Fig. 8(d). For the fresh catalyst, the peak located at 530.05 eV could be ascribed to iron oxide [83]. The binding energy at 531.7 eV is ascribed to the surface O—H group [84]. After reaction with PMS, the peak intensity of surface O—H group increased. The variations of O 1s XPS spectrum in the fresh and used catalyst indicated that more surface O—H group generated and participated in catalytic activation of PMS.

$$\equiv Fe(III) + H_2O \rightarrow \equiv Fe(III) - OH + H^+ \quad (13)$$

$$\equiv Fe(III) - OH + HSO_5^- \rightarrow \equiv Fe(II) - OH + SO_5^{\cdot -} + H^+ \quad (14)$$

$$\equiv Fe(II) - OH + HSO_5^- \rightarrow \equiv Fe(III) - OH + SO_4^{\cdot -} + OH^- \quad (15)$$

According to the above results and discussions, a possible mechanism was proposed for heterogeneous degradation of ATZ in the PS-Fe_2O_3-2/PMS system. As shown in Fig. 9, the formation of reactive radicals was tightly related to the oxidation of low-valent sulfur species (sulfite) and the iron redox cycle on the surface of the catalyst. Firstly, ≡Fe(III) or ≡Fe(II) on the surface of PS-Fe_2O_3-2 could active PMS to produce $SO_5^{\cdot -}$ and $SO_4^{\cdot -}$ via Eqs.(16) and (17). Secondly, it was reported that sulfur doped in hematite could accelerate electron transfer between the peroxide species/persulfate and Fe_2O_3 [41,43]. Meanwhile, the consumption of surface doped sulfite would promote the regeneration of ≡Fe(II) from lattice ≡Fe(III), accelerating the Fe(II)-mediated PMS activation. Thirdly, with the consumption and loss of sulfur species on the surface of iron oxides, more hydroxyl groups were formed on the surface of catalyst, forming the Fe—OH reactive sites and ligands to facilitate PMS activation for ATZ degradation (Eqs. (13)–(15)) [23,55]. In addition, ·OH could be further produced through H_2O/OH^- oxidation by $SO_4^{\cdot -}$ (Eqs. (18) and (19)).

$$\equiv Fe(III) + HSO_5^- \rightarrow \equiv Fe(II) + SO_5^{\cdot -} + H^+ \quad (16)$$

$$\equiv Fe(II) + HSO_5^- \rightarrow \equiv Fe(III) + SO_4^{\cdot -} + OH^- \quad (17)$$

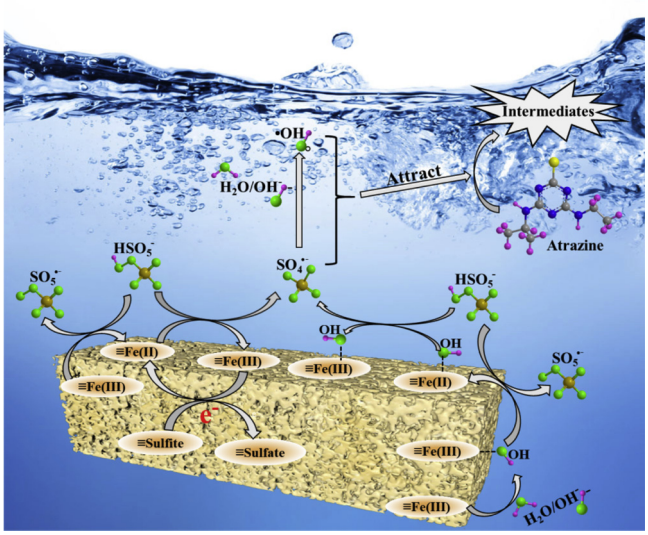

Fig. 9. The possible mechanism of PMS activation and ATZ degradation in the PS-Fe_2O_3-2/PMS system.

$$SO_4^{\cdot -} + H_2O \rightarrow SO_4^{2-} + {}^{\cdot}OH + H^+ \quad (18)$$

$$SO_4^{\cdot -} + OH^- \rightarrow SO_4^{2-} + {}^{\cdot}OH \quad (19)$$

3.8.2. Stability of the PS-Fe_2O_3-2 catalyst

To explore the stability, the PS-Fe_2O_3-2 was recycled with an external magnetic field, and reused for the succeeding degradation experiments in the conditions of 0.4 g·L^{-1} PS-Fe_2O_3-2, 0.6 mM PMS, 5 μM ATZ, and pH = 7.0. As seen in Fig S14a, the activity of PS-Fe_2O_3-2 slightly decreased for the second run, and obviously reduced for the third run in 40 min. The catalyst activity decreased after reuse may be due to the following reasons. Firstly, the survey XPS spectra results (Fig. S12) showed that the contents of Fe and S in PS-Fe_2O_3-2 after use were reduced, which would lead to the decrease of active sites in the PS-Fe_2O_3-2. Secondly, the catalytic performance of PS-Fe_2O_3-2 in the PS-Fe_2O_3-2/PMS system (containing 10 mM phosphate buffer to control the neutral pH) could be obviously suppressed by phosphate ions (Fig. S5a), which was consistent with the previous reported results [33,57]. However, 96% of ATZ could be removed in the second run when the reaction time prolonged to 90 min. Furthermore, the leached Fe ions from PS-Fe_2O_3-2 in the 1 st, 2nd, 3rd run within 90 min was 2.2, 1.4, and 0.8 mg L^{-1}, respectively (Fig. S14b). Given the negligible role of the leached Fe/PMS system on the removal of ATZ (Fig. 4), and about 90% of ATZ removal in 90 min after the third run, the PS-Fe_2O_3-2 catalyst exerted acceptable stability and reusability by magnetic separation.

3.9. ATZ degradation intermediates and biotoxicity

3.9.1. Identification of ATZ degradation intermediates

During the ATZ degradation in the PS-Fe_2O_3-2/PMS system, eleven degradation intermediates were detected by LC–MS. Details of these intermediates are presented in Table S5, including *m/z* values, molecular formulas, chemical names, abbreviations, and molecular structures. Based on these detected products and previously reported results [2,85,86], two possible transformation pathways of ATZ in the PS-Fe_2O_3-2/PMS system are proposed as illustrated in Fig. 10, namely lateral chain oxidation and dechlorination-hydroxylation routes.

Lateral chain oxidation takes place on the alkylamino groups of ATZ, including alkylic-hydroxylation, alkylic-oxidation, dealkylation, and olefination processes. Generally, reactive species tend to attack the ethylamino and iso-propylamin lateral chains of ATZ via H-abstraction [85]. The lateral chain oxidation was initialized by the formation of C-centered radical on the α-C adjacent to N atom through α-H abstraction by ·OH and/or $SO_4^{\cdot -}$ [2,19,86]. Subsequently, the carbon-centered radical would undergo the following steps, which are depicted in Fig. 10. Firstly, ·OH could attack the carbon-centered radical to produce alkylic-hydroxylation by-products [85,86], namely CNIT (*m/z* 232.095) or isomer CEHT (*m/z* 232.095), which further underwent dehydration process resulting in olefination by-products [85], such as CVIT (*m/z* 214.085) or isomer CEPT (*m/z* 214.085). Secondly, the carbon-centered radical could also be attacked by a peroxide radical generated from dissolved oxygen, leading to the formation of olefination intermediates with an imine group on the lateral chain of ATZ through loss of a perhydroxyl radical ($HO_2^{\cdot}$) [2,86], such as CVIT (*m/z* 214.085) or isomer CEPT (*m/z* 214.085), OVIT (*m/z* 196.119) and CVAT (*m/z* 172.038). Then, the imine group can be eventually hydrolyzed to dealkylation products [2,85,86], such as DEA (*m/z* 188.069), DIA (*m/z* 174.054), CAAT (*m/z* 146.022) and OAIT (*m/z* 170.103). In addition, $SO_4^{\cdot -}$ and/or ·OH could attack hydroxide group in CNIT (*m/z* 232.095) through H-abstraction, leading to the formation of aldehyde byproduct, CDIT (*m/z* 230.080) [2,86], which could be further oxidized to dealkylation transformation product (CDAT (*m/z* 188.096)) [85].

Dechlorination-hydroxylation process was another degradation pathway during ATZ degradation. $SO_4^{\cdot -}$/·OH could react with ATZ via electron transfer to generate ATZ radicals ($[C_8H_{14}ClN_5]^{\cdot}$) [2,86]. Then, dechlorinated-hydroxylated derivatives were generated by replacing chlorine atoms with hydroxyl groups. In this study, it is worth noting that ODIT (*m/z* 212.114) was transformed from CDIT (*m/z* 230.080) through a dechlorination-hydroxylation process [2]. Besides, ODIT could process olefination to yield OVIT (*m/z* 196.119), which could further go through dealkylation process to generate OAIT (*m/z* 170.103).

3.9.2. Biotoxicity assessment of ATZ solution during the reaction

The potential biotoxicity of ATZ degradation solution in the PS-Fe_2O_3-2/PMS system was evaluated by activated sludge inhibition test [57]. The samples were collected at different reaction times during the treatment process (up to 40 min). As can be seen from Fig. S15, the inhibition of oxygen uptake rate by activated sludge decreased rapidly from 37% to 26% in the first 10 min, and then slowly decreased from 26% to 23% in the next 10 min, followed by a significantly drop from 37% to 9% in the last 20 min. The gradual decrease of the inhibition of oxygen uptake rate implies that ATZ was degraded and mineralized to the less toxic byproducts by the PS-Fe_2O_3-2/PMS system. As reported, the detected ATZ degradation by-products, such as DEA (*m/z* 188.069), DIA (*m/z* 174.054), CAAT (*m/z* 146.022) and dechlorination-hydroxylation derivatives [57,85,87], have a lower toxicity than ATZ. The results suggested that the PS-Fe_2O_3-2/PMS system has potential to reduce the toxicity of ATZ contaminated wastewater.

4. Conclusions

In this work, PS-Fe_2O_3 material with porous structure and good magnetism was prepared. Compared to non-modified Fe_2O_3, PS-Fe_2O_3 exhibited superior performance in the heterogeneous activation of PMS for ATZ degradation in neutral condition. With increase of catalyst dose, PMS concentration and extent of sulfur modification of catalyst, the ATZ removal efficiency was markedly enhanced. The best performance of PS-Fe_2O_3-2/PMS system was observed at neutral and slightly alkaline conditions. Low-valent sulfur species (sulfite) on the surface of catalyst generated by thiosulfate induced sulfur-modification could accelerate ≡Fe(II) regeneration via electron transfer, which enhanced degradation efficiency of PS-Fe_2O_3-2/PMS system. The presence of Cl^-, HCO_3^-, NO_3^- and HA presented inhibition effects on ATZ removal. Moreover, both $SO_4^{\cdot -}$ and ·OH were identified in this system, while $SO_4^{\cdot -}$ played a dominant role in ATZ degradation. Additionally, eleven transformation products were produced during the degradation of ATZ through lateral chain oxidation and dechlorination-hydroxylation

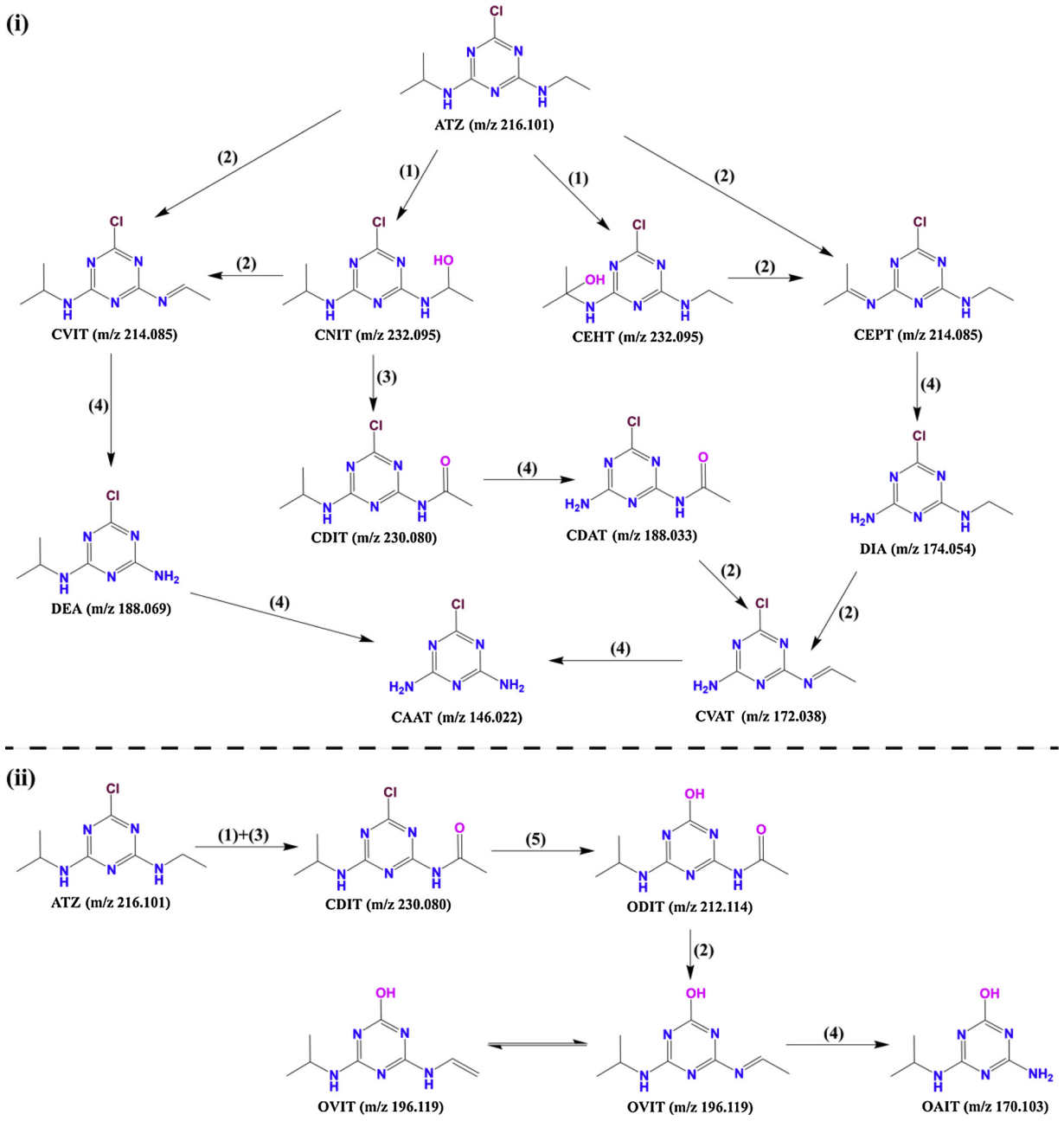

Fig. 10. Proposed degradation pathway of ATZ in the PS-Fe_2O_3-2/PMS system: (1) alkylic-hydroxylation, (2) olefination, (3) alkylic-oxidation, (4) de-alkylation, (5) dechlorination-hydroxylation.

processes in the PS-Fe_2O_3-2/PMS system. Furthermore, the biotoxicity evaluation suggested that ATZ was effectively eliminated and the biological toxicity decreased, indicating PS-Fe_2O_3-2/PMS as an effective and promising treatment technology for the ATZ contaminated wastewater.

Acknowledgements

This research is financed by the Natural Science Foundation of China (41373083 and 41611130185), the Natural Science Foundation of Hubei Province (2018045023). Ying Huang acknowledges support from the China Scholarship Council (CSC) scholarship (201306270057). D. D. Dionysiou also acknowledges support from the University of Cincinnati through a UNESCO co-Chair Professor position on “Water Access and Sustainability” and the Herman Schneider Professorship in the College of Engineering and Applied Sciences.

Appendix A. Supplementary data

Supplementary material related to this article can be found, in the online version, at doi:https://doi.org/10.1016/j.apcatb.2019.118056.

References

[1] N. Graziano, M.J. McGuire, A. Roberson, C. Adams, H. Jiang, N. Blute, National atrazine occurrence monitoring program using the abraxis ELISA method, Environ. Sci. Technol. 40 (2006) (2004) 1163–1171, https://doi.org/10.1021/es051586y.
[2] Y. Ji, C. Dong, D. Kong, J. Lu, Q. Zhou, Heat-activated persulfate oxidation of atrazine: implications for remediation of groundwater contaminated by herbicides, Chem. Eng. J. 263 (2015) 45–54, https://doi.org/10.1016/j.cej.2014.10.097.
[3] H. Tyrone, H. Kelly, T. Mable, H. Anhthu, H. Cathryn, V. Aaron, Herbicides: feminization of male frogs in the wild, Nature 419 (2002) 895, https://doi.org/10.1038/419895a.
[4] A. Gely-Pernot, C. Hao, E. Becker, I. Stuparevic, C. Kervarrec, F. Chalmel, M. Primig, B. Jégou, F. Smagulova, The epigenetic processes of meiosis in male mice

are broadly affected by the widely used herbicide atrazine, BMC Genomics 16 (2015) 885, https://doi.org/10.1186/s12864-015-2095-y.
[5] H. Zhang, X. Liu, J. Ma, C. Lin, C. Qi, X. Li, Z. Zhou, G. Fan, Activation of peroxymonosulfate using drinking water treatment residuals for the degradation of atrazine, J. Hazard. Mater. 344 (2018) 1220–1228, https://doi.org/10.1016/j.jhazmat.2017.11.038.
[6] J. Cheng, M. Liu, X. Zhang, L. Ding, Y. Yu, X. Wang, H. Jin, H. Zhang, Determination of triazine herbicides in sheep liver by microwave-assisted extraction and high performance liquid chromatography, Anal. Chim. Acta 590 (2007) 34–39, https://doi.org/10.1016/j.aca.2007.03.017.
[7] A. Claver, P. Ormad, L. Rodríguez, J.L. Ovelleiro, Study of the presence of pesticides in surface waters in the Ebro river basin (Spain), Chemosphere 64 (2006) 1437–1443, https://doi.org/10.1016/j.chemosphere.2006.02.034.
[8] Q. Li, Y. Luo, J. Song, L. Wu, Risk assessment of atrazine polluted farmland and drinking water: a case study, Bull. Environ. Contam. Toxicol. 78 (2007) 187–190, https://doi.org/10.1007/s00128-007-9051-8.
[9] M. Qu, H. Li, N. Li, G. Liu, J. Zhao, Y. Hua, D. Zhu, Distribution of atrazine and its phytoremediation by submerged macrophytes in lake sediments, Chemosphere 168 (2017) 1515–1522, https://doi.org/10.1016/j.chemosphere.2016.11.164.
[10] S. Wu, H. He, X. Inthapanya, C. Yang, L. Lu, G. Zeng, Z. Han, Role of biochar on composting of organic wastes and remediation of contaminated soils—a review, Environ. Sci. Pollut. Res. – Int. 24 (2017) 16560–16577, https://doi.org/10.1007/s11356-017-9168-1.
[11] A.L. Ahmad, L.S. Tan, S.R.A. Shukor, Dimethoate and atrazine retention from aqueous solution by nanofiltration membranes, J. Hazard. Mater. 151 (2008) 71–77, https://doi.org/10.1016/j.jhazmat.2007.05.047.
[12] X. Cheng, H. Liang, A. Ding, X. Tang, B. Liu, X. Zhu, Z. Gan, D. Wu, G. Li, Ferrous iron/peroxymonosulfate oxidation as a pretreatment for ceramic ultrafiltration membrane: control of natural organic matter fouling and degradation of atrazine, Water Res. 113 (2017) 32–41, https://doi.org/10.1016/j.watres.2017.01.055.
[13] C. Zhu, W.L. Yang, H. He, C. Yang, J. Yu, X. Wu, G. Zeng, S. Tarre, M. Green, Preparation, performances and mechanisms of magnetic Saccharomyces cerevisiae bionanocomposites for atrazine removal, Chemosphere 200 (2018) 380–387, https://doi.org/10.1016/j.chemosphere.2018.02.020.
[14] J. Yu, H. He, W.L. Yang, C. Yang, G. Zeng, X. Wu, Magnetic bionanoparticles of Penicillium sp. yz11-22N2 doped with Fe_3O_4 and encapsulated within PVA-SA gel beads for atrazine removal, Bioresour. Technol. 260 (2018) 196–203, https://doi.org/10.1016/j.biortech.2018.03.103.
[15] W.-D. Oh, Z. Dong, T.-T. Lim, Generation of sulfate radical through heterogeneous catalysis for organic contaminants removal: current development, challenges and prospects, Appl. Catal. B: Environ. 194 (2016) 169–201, https://doi.org/10.1016/j.apcatb.2016.04.003.
[16] R. Xiao, Z. Luo, Z. Wei, S. Luo, R. Spinney, W. Yang, D.D. Dionysiou, Activation of peroxymonosulfate/persulfate by nanomaterials for sulfate radical-based advanced oxidation technologies, Curr. Opin. Chem. Eng. 19 (2018) 51–58, https://doi.org/10.1016/j.coche.2017.12.005.
[17] S. Wacławek, H.V. Lutze, K. Grübel, V.V.T. Padil, M. Černík, D.D. Dionysiou, Chemistry of persulfates in water and wastewater treatment: a review, Chem. Eng. J. 330 (2017) 44–62, https://doi.org/10.1016/j.cej.2017.07.132.
[18] G.-X. Huang, C.-Y. Wang, C.-W. Yang, P.-C. Guo, H.-Q. Yu, Degradation of bisphenol a by peroxymonosulfate catalytically activated with $Mn_{1.8}Fe_{1.2}O_4$ nanospheres: synergism between Mn and Fe, Environ. Sci. Technol. 51 (2017) 12611–12618, https://doi.org/10.1021/acs.est.7b03007.
[19] H.V. Lutze, S. Bircher, I. Rapp, N. Kerlin, R. Bakkour, M. Geisler, C. von Sonntag, T.C. Schmidt, Degradation of chlorotriazine pesticides by sulfate radicals and the influence of organic matter, Environ. Sci. Technol. 49 (2015) 1673–1680, https://doi.org/10.1021/es503496u.
[20] J. Wang, S. Wang, Activation of persulfate (PS) and peroxymonosulfate (PMS) and application for the degradation of emerging contaminants, Chem. Eng. J. 334 (2018) 1502–1517, https://doi.org/10.1016/j.cej.2017.11.059.
[21] F. Ghanbari, M. Moradi, Application of peroxymonosulfate and its activation methods for degradation of environmental organic pollutants: review, Chem. Eng. J. 310 (2017) 41–62, https://doi.org/10.1016/j.cej.2016.10.064.
[22] G.P. Anipsitakis, D.D. Dionysiou, Radical generation by the interaction of transition metals with common oxidants, Environ. Sci. Technol. 38 (2004) 3705–3712, https://doi.org/10.1021/es035121o.
[23] Y. Ren, L. Lin, J. Ma, J. Yang, J. Feng, Z. Fan, Sulfate radicals induced from peroxymonosulfate by magnetic ferrospinel MFe_2O_4 (M= Co, Cu, Mn, and Zn) as heterogeneous catalysts in the water, Appl. Catal. B: Environ. 165 (2015) 572–578, https://doi.org/10.1016/j.apcatb.2014.10.051.
[24] F. Jiang, B. Qiu, D. Sun, Advanced degradation of refractory pollutants in incineration leachate by UV/peroxymonosulfate, Chem. Eng. J. 349 (2018) 338–346, https://doi.org/10.1016/j.cej.2018.05.062.
[25] J. Liu, J. Zhou, Z. Ding, Z. Zhao, X. Xu, Z. Fang, Ultrasound irritation enhanced heterogeneous activation of peroxymonosulfate with Fe_3O_4 for degradation of azo dye, Ultrason. Sonochem. 34 (2017) 953–959, https://doi.org/10.1016/j.ultsonch.2016.08.005.
[26] M. Wei, L. Gao, J. Li, J. Fang, W. Cai, X. Li, A. Xu, Activation of peroxymonosulfate by graphitic carbon nitride loaded on activated carbon for organic pollutants degradation, J. Hazard. Mater. 316 (2016) 60–68, https://doi.org/10.1016/j.jhazmat.2016.05.031.
[27] E.-T. Yun, J.H. Lee, J. Kim, H.-D. Park, J. Lee, Identifying the nonradical mechanism in the peroxymonosulfate activation process: singlet oxygenation versus mediated Electron transfer, Environ. Sci. Technol. 52 (2018) 7032–7042, https://doi.org/10.1021/acs.est.8b00959.
[28] C. Qi, X. Liu, J. Ma, C. Lin, X. Li, H. Zhang, Activation of peroxymonosulfate by base: implications for the degradation of organic pollutants, Chemosphere 151 (2016) 280–288, https://doi.org/10.1016/j.chemosphere.2016.02.089.
[29] X. Lou, L. Wu, Y. Guo, C. Chen, Z. Wang, D. Xiao, C. Fang, J. Liu, J. Zhao, S. Lu, Peroxymonosulfate activation by phosphate anion for organics degradation in water, Chemosphere 117 (2014) 582–585, https://doi.org/10.1016/j.chemosphere.2014.09.046.
[30] X. Lou, C. Fang, Z. Geng, Y. Jin, D. Xiao, Z. Wang, J. Liu, Y. Guo, Significantly enhanced base activation of peroxymonosulfate by polyphosphates: kinetics and mechanism, Chemosphere 173 (2017) 529–534, https://doi.org/10.1016/j.chemosphere.2017.01.093.
[31] A.B. Cundy, L. Hopkinson, R.L.D. Whitby, Use of iron-based technologies in contaminated land and groundwater remediation: a review, Sci. Total Environ. 400 (2008) 42–51, https://doi.org/10.1016/j.scitotenv.2008.07.002.
[32] E. Stephan, J. Kathrin, B. Matthias, Sustainable metal catalysis with iron: from rust to a rising star? Angew. Chem. Int. Ed. 47 (2010) 3317–3321, https://doi.org/10.1002/anie.200800012.
[33] N. Jaafarzadeh, F. Ghanbari, M. Ahmadi, Catalytic degradation of 2,4-dichlorophenoxyacetic acid (2,4-D) by nano-Fe_2O_3 activated peroxymonosulfate: Influential factors and mechanism determination, Chemosphere 169 (2017) 568–576, https://doi.org/10.1016/j.chemosphere.2016.11.038.
[34] C. Tan, N. Gao, Y. Deng, J. Deng, S. Zhou, J. Li, X. Xin, Radical induced degradation of acetaminophen with Fe_3O_4 magnetic nanoparticles as heterogeneous activator of peroxymonosulfate, J. Hazard. Mater. 276 (2014) 452–460, https://doi.org/10.1016/j.jhazmat.2014.05.068.
[35] C. Tan, Y. Dong, D. Fu, N. Gao, J. Ma, X. Liu, Chloramphenicol removal by zero valent iron activated peroxymonosulfate system: kinetics and mechanism of radical generation, Chem. Eng. J. 334 (2018) 1006–1015, https://doi.org/10.1016/j.cej.2017.10.020.
[36] F. Ji, C. Li, X. Wei, J. Yu, Efficient performance of porous Fe_2O_3 in heterogeneous activation of peroxymonosulfate for decolorization of Rhodamine B, Chem. Eng. J. 231 (2013) 434–440, https://doi.org/10.1016/j.cej.2013.07.053.
[37] W.-D. Oh, S.K. Lua, Z. Dong, T.-T. Lim, High surface area DPA-hematite for efficient detoxification of bisphenol A via peroxymonosulfate activation, J. Mater. Chem. A 2 (2014) 15836–15845, https://doi.org/10.1039/C4TA02758B.
[38] D. Fan, Y. Lan, P.G. Tratnyek, R.L. Johnson, J. Filip, D.M. O'Carroll, A. Nunez Garcia, A. Agrawal, Sulfidation of iron-based materials: a review of processes and implications for water treatment and remediation, Environ. Sci. Technol. 51 (2017) 13070–13085, https://doi.org/10.1021/acs.est.7b04177.
[39] J. Li, X. Zhang, Y. Sun, L. Liang, B. Pan, W. Zhang, X. Guan, Advances in sulfidation of zerovalent Iron for water decontamination, Environ. Sci. Technol. 51 (2017) 13533–13544, https://doi.org/10.1021/acs.est.7b02695.
[40] C. Xia, Y. Jia, M. Tao, Q. Zhang, Tuning the band gap of hematite α-Fe_2O_3 by sulfur doping, Phys. Lett. A 377 (2013) 1943–1947, https://doi.org/10.1016/j.physleta.2013.05.026.
[41] L. Guo, F. Chen, X. Fan, W. Cai, J. Zhang, S-doped α-Fe_2O_3 as a highly active heterogeneous Fenton-like catalyst towards the degradation of acid orange 7 and phenol, Appl. Catal. B: Environ. 96 (2010) 162–168, https://doi.org/10.1016/j.apcatb.2010.02.015.
[42] J. Du, J. Bao, X. Fu, C. Lu, S.H. Kim, Mesoporous sulfur-modified iron oxide as an effective Fenton-like catalyst for degradation of bisphenol A, Appl. Catal. B: Environ. 184 (2016) 132–141, https://doi.org/10.1016/j.apcatb.2015.11.015.
[43] J. Du, J. Bao, X. Fu, C. Lu, S.H. Kim, Facile preparation of S/Fe composites as an effective peroxydisulfate activator for RhB degradation, Sep. Purif. Technol. 163 (2016) 145–152, https://doi.org/10.1016/j.seppur.2016.02.051.
[44] J. Li, Q. Liu, Q. qing Ji, B. Lai, Degradation of p-nitrophenol (PNP) in aqueous solution by Fe^0-PM-PS system through response surface methodology (RSM), Appl. Catal. B: Environ. 200 (2017) 633–646, https://doi.org/10.1016/j.apcatb.2016.07.026.
[45] H. Bahrami, A. Eslami, R. Nabizadeh, A. Mohseni-Bandpi, A. Asadi, M. Sillanpää, Degradation of trichloroethylene by sonophotolytic-activated persulfate processes: optimization using response surface methodology, J. Clean. Prod. 198 (2018) 1210–1218, https://doi.org/10.1016/j.jclepro.2018.07.100.
[46] R. Khaghani, B. Kakavandi, K. Ghadirinejad, E. Dehghani Fard, A. Asadi, Preparation, characterization and catalytic potential of γ-Fe_2O_3@AC mesoporous heterojunction for activation of peroxymonosulfate into degradation of cyfluthrin insecticide, Microporous Mesoporous Mater. 284 (2019) 111–121, https://doi.org/10.1016/j.micromeso.2019.04.013.
[47] J. Du, J. Bao, C. Lu, D. Werner, Reductive sequestration of chromate by hierarchical FeS@Fe^0 particles, Water Res. 102 (2016) 73–81, https://doi.org/10.1016/j.watres.2016.06.009.
[48] Y. El Mendili, J.-F. Bardeau, N. Randrianantoandro, A. Gourbil, J.-M. Greneche, A.-M. Mercier, F. Grasset, New evidences of in situ laser irradiation effects on γ-Fe_2O_3 nanoparticles: a Raman spectroscopic study, JRSp 42 (2011) 239–242, https://doi.org/10.1002/jrs.2762.
[49] Y.-S. Li, J.S. Church, A.L. Woodhead, Infrared and Raman spectroscopic studies on iron oxide magnetic nano-particles and their surface modifications, J. Magn. Magn. Mater. 324 (2012) 1543–1550, https://doi.org/10.1016/j.jmmm.2011.11.065.
[50] L. Zhao, X. Li, C. Hao, C.L. Raston, SO_2adsorption and transformation on calcined NiAl hydrotalcite-like compounds surfaces: An in situ FTIR and DFT study, Appl. Catal. B: Environ. 117-118 (2012) 339–345, https://doi.org/10.1016/j.apcatb.2012.01.034.
[51] Z. Zhang, J. Huang, H. Xia, Q. Dai, Y. Gu, Y. Lao, X. Wang, Chlorinated volatile organic compound oxidation over SO_4^{2-}/Fe_2O_3 catalysts, J. Catal. 360 (2018) 277–289, https://doi.org/10.1016/j.jcat.2017.11.024.
[52] A.M. Banerjee, A.R. Shirole, M.R. Pai, A.K. Tripathi, S.R. Bharadwaj, D. Das, P.K. Sinha, Catalytic activities of Fe_2O_3 and chromium doped Fe_2O_3 for sulfuric acid

decomposition reaction in an integrated boiler, preheater, and catalytic decomposer, Appl. Catal. B: Environ. 127 (2012) 36–46, https://doi.org/10.1016/j.apcatb.2012.07.030.
[53] L. Notini, D.E. Latta, A. Neumann, C.I. Pearce, M. Sassi, A.T. N'Diaye, K.M. Rosso, M.M. Scherer, The role of defects in Fe(II)–goethite electron transfer, Environ. Sci. Technol. 52 (2018) 2751–2759, https://doi.org/10.1021/acs.est.7b05772.
[54] Y. Feng, D. Wu, Y. Deng, T. Zhang, K. Shih, Sulfate radical-mediated degradation of sulfadiazine by $CuFeO_2$ rhombohedral crystal-catalyzed peroxymonosulfate: synergistic effects and mechanisms, Environ. Sci. Technol. 50 (2016) 3119–3127, https://doi.org/10.1021/acs.est.5b05974.
[55] Y. Xu, J. Ai, H. Zhang, The mechanism of degradation of bisphenol A using the magnetically separable $CuFe_2O_4$/peroxymonosulfate heterogeneous oxidation process, J. Hazard. Mater. 309 (2016) 87–96, https://doi.org/10.1016/j.jhazmat.2016.01.023.
[56] C. Chen, F. Duan, S. Zhao, W. Wang, F. Yang, W. Nuansing, B. Zhang, Y. Qin, M. Knez, Porous Fe_2O_3 nanotubes with α-γ phase junction for enhanced charge separation and photocatalytic property produced by molecular layer deposition, Appl. Catal. B: Environ. 248 (2019) 218–225, https://doi.org/10.1016/j.apcatb.2019.02.029.
[57] J. Li, M. Xu, G. Yao, B. Lai, Enhancement of the degradation of atrazine through $CoFe_2O_4$ activated peroxymonosulfate (PMS) process: kinetic, degradation intermediates, and toxicity evaluation, Chem. Eng. J. 348 (2018) 1012–1024, https://doi.org/10.1016/j.cej.2018.05.032.
[58] C. Tan, X. Jian, Y. Dong, X. Lu, X. Liu, H. Xiang, X. Cui, J. Deng, H. Gao, Activation of peroxymonosulfate by a novel EGCE@Fe_3O_4 nanocomposite: free radical reactions and implication for the degradation of sulfadiazine, Chem. Eng. J. 359 (2019) 594–603, https://doi.org/10.1016/j.cej.2018.11.178.
[59] T. Zhang, H. Zhu, J.-P. Croué, Production of sulfate radical from peroxymonosulfate induced by a magnetically separable $CuFe_2O_4$ spinel in water: efficiency, stability, and mechanism, Environ. Sci. Technol. 47 (2013) 2784–2791, https://doi.org/10.1021/es304721g.
[60] T. Dombek, E. Dolan, J. Schultz, D. Klarup, Rapid reductive dechlorination of atrazine by zero-valent iron under acidic conditions, Environ. Pollut. 111 (2001) 21–27, https://doi.org/10.1016/S0269-7491(00)00033-6.
[61] S. Wu, H. He, X. Li, C. Yang, G. Zeng, B. Wu, S. He, L. Lu, Insights into atrazine degradation by persulfate activation using composite of nanoscale zero-valent iron and graphene: performances and mechanisms, Chem. Eng. J. 341 (2018) 126–136, https://doi.org/10.1016/j.cej.2018.01.136.
[62] T. Zhou, X. Zou, J. Mao, X. Wu, Decomposition of sulfadiazine in a sonochemical Fe^0-catalyzed persulfate system: parameters optimizing and interferences of wastewater matrix, Appl. Catal. B: Environ. 185 (2016) 31–41, https://doi.org/10.1016/j.apcatb.2015.12.004.
[63] A. Khan, S. Zou, T. Wang, J. Ifthikar, A. Jawad, Z. Liao, A. Shahzad, A. Ngambia, Z. Chen, Facile synthesis of yolk shell Mn_2O_3@Mn_5O_8 as an effective catalyst for peroxymonosulfate activation, PCCP 20 (2018) 13909–13919, https://doi.org/10.1039/C8CP02080A.
[64] R. Yuan, S.N. Ramjaun, Z. Wang, J. Liu, Effects of chloride ion on degradation of Acid Orange 7 by sulfate radical-based advanced oxidation process: implications for formation of chlorinated aromatic compounds, J. Hazard. Mater. 196 (2011) 173–179, https://doi.org/10.1016/j.jhazmat.2011.09.007.
[65] L. Chen, S. Yang, X. Zuo, Y. Huang, T. Cai, D. Ding, Biochar modification significantly promotes the activity of Co_3O_4 towards heterogeneous activation of peroxymonosulfate, Chem. Eng. J. 354 (2018) 856–865, https://doi.org/10.1016/j.cej.2018.08.098.
[66] P. Hu, M. Long, Cobalt-catalyzed sulfate radical-based advanced oxidation: a review on heterogeneous catalysts and applications, Appl. Catal. B: Environ. 181 (2016) 103–117, https://doi.org/10.1016/j.apcatb.2015.07.024.
[67] J. Ma, N.J.D. Graham, Degradation of atrazine by manganese-catalysed ozonation—influence of radical scavengers, Water Res. 34 (2000) 3822–3828, https://doi.org/10.1016/S0043-1354(00)00130-5.
[68] Y.-H. Guan, J. Ma, Y.-M. Ren, Y.-L. Liu, J.-Y. Xiao, L.-q. Lin, C. Zhang, Efficient degradation of atrazine by magnetic porous copper ferrite catalyzed peroxymonosulfate oxidation via the formation of hydroxyl and sulfate radicals, Water Res. 47 (2013) 5431–5438, https://doi.org/10.1016/j.watres.2013.06.023.
[69] C. Li, H. Lin, A. Armutlulu, R. Xie, Y. Zhang, X. Meng, Hydroxylamine-assisted catalytic degradation of ciprofloxacin in ferrate/persulfate system, Chem. Eng. J. 360 (2019) 612–620, https://doi.org/10.1016/j.cej.2018.11.218.
[70] J.M. Fontmorin, R.C. Burgos Castillo, W.Z. Tang, M. Sillanpää, Stability of 5,5-dimethyl-1-pyrroline-N-oxide as a spin-trap for quantification of hydroxyl radicals in processes based on Fenton reaction, Water Res. 99 (2016) 24–32, https://doi.org/10.1016/j.watres.2016.04.053.
[71] Y. Wang, H. Sun, H.M. Ang, M.O. Tadé, S. Wang, 3D-hierarchically structured MnO_2 for catalytic oxidation of phenol solutions by activation of peroxymonosulfate: structure dependence and mechanism, Appl. Catal. B: Environ. 164 (2015) 159–167, https://doi.org/10.1016/j.apcatb.2014.09.004.
[72] M. Xie, J. Tang, L. Kong, W. Lu, V. Natarajan, F. Zhu, J. Zhan, Cobalt doped g-C_3N_4 activation of peroxymonosulfate for monochlorophenols degradation, Chem. Eng. J. 360 (2019) 1213–1222, https://doi.org/10.1016/j.cej.2018.10.130.
[73] H. Li, J. Tian, Z. Zhu, F. Cui, Y.-A. Zhu, X. Duan, S. Wang, Magnetic nitrogen-doped nanocarbons for enhanced metal-free catalytic oxidation: integrated experimental and theoretical investigations for mechanism and application, Chem. Eng. J. 354 (2018) 507–516, https://doi.org/10.1016/j.cej.2018.08.043.
[74] P. Shao, J. Tian, X. Duan, Y. Yang, W. Shi, X. Luo, F. Cui, S. Luo, S. Wang, Cobalt silicate hydroxide nanosheets in hierarchical hollow architecture with maximized cobalt active site for catalytic oxidation, Chem. Eng. J. 359 (2019) 79–87, https://doi.org/10.1016/j.cej.2018.11.121.
[75] G. Liu, X. Li, B. Han, L. Chen, L. Zhu, L.C. Campos, Efficient degradation of sulfamethoxazole by the Fe(II)/HSO_5^- process enhanced by hydroxylamine: efficiency and mechanism, J. Hazard. Mater. 322 (2017) 461–468, https://doi.org/10.1016/j.jhazmat.2016.09.062.
[76] H. Chi, X. He, J. Zhang, D. Wang, X. Zhai, J. Ma, Hydroxylamine enhanced degradation of naproxen in Cu^{2+} activated peroxymonosulfate system at acidic condition: efficiency, mechanisms and pathway, Chem. Eng. J. 361 (2019) 764–772, https://doi.org/10.1016/j.cej.2018.12.114.
[77] Q. Yi, L. Bu, Z. Shi, S. Zhou, Epigallocatechin-3-gallate-coated Fe_3O_4 as a novel heterogeneous catalyst of peroxymonosulfate for diuron degradation: performance and mechanism, Chem. Eng. J. 302 (2016) 417–425, https://doi.org/10.1016/j.cej.2016.05.025.
[78] E. Saputra, S. Muhammad, H. Sun, H.-M. Ang, M.O. Tadé, S. Wang, Manganese oxides at different oxidation states for heterogeneous activation of peroxymonosulfate for phenol degradation in aqueous solutions, Appl. Catal. B: Environ. 142-143 (2013) 729–735, https://doi.org/10.1016/j.apcatb.2013.06.004.
[79] Y. Zhou, X. Wang, C. Zhu, D.D. Dionysiou, G. Zhao, G. Fang, D. Zhou, New insight into the mechanism of peroxymonosulfate activation by sulfur-containing minerals: role of sulfur conversion in sulfate radical generation, Water Res. 142 (2018) 208–216, https://doi.org/10.1016/j.watres.2018.06.002.
[80] L. Xu, J. Wang, Magnetic nanoscaled Fe_3O_4/CeO_2 composite as an efficient fenton-like heterogeneous catalyst for degradation of 4-chlorophenol, Environ. Sci. Technol. 46 (2012) 10145–10153, https://doi.org/10.1021/es300303f.
[81] T. Yamashita, P. Hayes, Analysis of XPS spectra of Fe^{2+} and Fe^{3+} ions in oxide materials, Appl. Surf. Sci. 254 (2008) 2441–2449, https://doi.org/10.1016/j.apsusc.2007.09.063.
[82] P. Bonnissel-Gissinger, M. Alnot, J.-J. Ehrhardt, P. Behra, Surface oxidation of pyrite as a function of pH, Environ. Sci. Technol. 32 (1998) 2839–2845, https://doi.org/10.1021/es980213c.
[83] X. Lu, Y. Zeng, M. Yu, T. Zhai, C. Liang, S. Xie, M.S. Balogun, Y. Tong, Oxygen-deficient hematite nanorods as high-performance and novel negative electrodes for flexible asymmetric supercapacitors, Adv. Mater. 26 (2014) 3148–3155, https://doi.org/10.1002/adma.201305851.
[84] X. Ren, L. Chang, F. Li, K. Xie, Study of intrinsic sulfidation behavior of Fe_2O_3 for high temperature H_2S removal, Fuel 89 (2010) 883–887, https://doi.org/10.1016/j.fuel.2009.04.010.
[85] J.A. Khan, X. He, N.S. Shah, H.M. Khan, E. Hapeshi, D. Fatta-Kassinos, D.D. Dionysiou, Kinetic and mechanism investigation on the photochemical degradation of atrazine with activated H_2O_2, $S_2O_8^{2-}$ and HSO_5^-, Chem. Eng. J. 252 (2014) 393–403, https://doi.org/10.1016/j.cej.2014.04.104.
[86] Y. Huang, C. Han, Y. Liu, M.N. Nadagouda, L. Machala, K.E. O'Shea, V.K. Sharma, D.D. Dionysiou, Degradation of atrazine by $Zn_xCu_{1-x}Fe_2O_4$ nanomaterial-catalyzed sulfite under UV–vis light irradiation: green strategy to generate $SO_4^{\bullet-}$, Appl. Catal. B: Environ. 221 (2018) 380–392, https://doi.org/10.1016/j.apcatb.2017.09.001.
[87] A.B. Baranda, A. Barranco, I.M. de Marañón, Fast atrazine photodegradation in water by pulsed light technology, Water Res. 46 (2012) 669–678, https://doi.org/10.1016/j.watres.2011.11.034.